



## Full length article

Structural damage and phase stability of  $\text{Al}_{0.3}\text{CoCrFeNi}$  high entropy alloy under high temperature ion irradiation

Tengfei Yang<sup>a,b,\*</sup>, Wei Guo<sup>c</sup>, Jonathan D. Poplawsky<sup>c</sup>, Dongyue Li<sup>d</sup>, Ling Wang<sup>e</sup>, Yao Li<sup>b</sup>, Wangyu Hu<sup>a</sup>, Miguel L. Crespillo<sup>e</sup>, Zhanfeng Yan<sup>f</sup>, Yong Zhang<sup>d</sup>, Yugang Wang<sup>f</sup>, Steven J. Zinkle<sup>b,e,\*\*</sup>

<sup>a</sup> College of Materials Science and Engineering, Hunan University, Changsha 410082, China

<sup>b</sup> Department of Nuclear Engineering, University of Tennessee, Knoxville, TN 37996, United States

<sup>c</sup> Center for Nanophase Materials Sciences, Oak Ridge National Laboratory, Oak Ridge, TN 37831, United States

<sup>d</sup> State Key Laboratory for Advanced Metals and Materials, University of Science and Technology Beijing, Beijing 100083, China

<sup>e</sup> Department of Materials Science & Engineering, University of Tennessee, Knoxville, TN 37996, United States

<sup>f</sup> State Key Laboratory of Nuclear Physics and Technology, Center for Applied Physics and Technology, Peking University, Beijing 100871, China

## ARTICLE INFO

## Article History:

Received 5 November 2019

Revised 25 January 2020

Accepted 30 January 2020

Available online 5 February 2020

## Keywords:

High entropy alloy

Irradiation effect

Structural damage

Phase stability

## ABSTRACT

An initially single phase high entropy alloy (HEA)  $\text{Al}_{0.3}\text{CoCrFeNi}$  was irradiated by 3 MeV Au ions to a fluence of  $6 \times 10^{15} \text{ cm}^{-2}$  ( $\sim 31 \text{ dpa}$  at damage peak) at four different temperatures ranging from 250 °C to 650 °C. Transmission electron microscopy (TEM) and Atom probe tomography (APT) were employed to study the evolution of structural damage and phase stability with irradiation temperature.  $\text{Al}_{0.3}\text{CoCrFeNi}$  exhibited a similar evolution of irradiation-induced defects with temperature as compared with conventional FCC alloys. At 250 °C and 350 °C, most of the visible irradiation-induced defects were faulted 1/3(111) dislocation loops. As the irradiation temperature increased to 500 °C, perfect 1/2(110) dislocation loops were observed along with the faulted loops. At the highest irradiation temperature 650 °C, only dislocation lines and networks could be observed. Regarding phase stability, the 3 MeV Au irradiation was observed to suppress the precipitation of (Ni, Al)-enriched nano clusters and the L12 ordered structure at irradiation temperatures 250 °C to 500 °C whereas precipitation of the B2 ordered structure was accelerated at 650 °C. This resulted in qualitatively opposite precipitation behavior between the ion irradiated damage region and unirradiated region at 500 °C and 650 °C. The opposite phase stability of the ion-irradiated damage region and unirradiated region at different temperatures is attributed to the competing effects of ballistic dissolution vs irradiation enhanced diffusion on precipitation.

© 2020 Acta Materialia Inc. Published by Elsevier Ltd. All rights reserved.

## 1. Introduction

Advanced nuclear energy systems, including next generation fission reactors and proposed fusion energy reactors, will operate in harsh environments involving intense neutron irradiation, high

temperatures, chemically reactive environments and large time-varying stresses [1–3]. The high dose neutron irradiation in aggressive environments can cause serious structural damage in materials, resulting in the degradation of mechanical properties, such as hardening, creep, volume swelling, etc. [4]. Therefore, a daunting and important challenge in the development of advanced nuclear energy systems is the exploration of advanced structural materials with higher performance that can endure high dose neutron irradiation under extreme environments [5,6].

Recently, high-entropy alloys (HEAs) have attracted tremendous attention because of their unique compositions, microstructures and favorable mechanical properties [7]. HEAs are generally defined as a multi-element solid solution composed of five or more principal elements in equimolar or near-equimolar ratios [8]. Due to the high configurational entropy and/or other factors, the formation of intermetallic phases may be restrained and HEAs tend to form simple structures like FCC (face-centered cubic) and BCC (body-centered

This manuscript has been authored by UT-Battelle, LLC under Contract No. DE-AC05-00OR22725 with the U.S. Department of Energy. The United States Government retains and the publisher, by accepting the article for publication, acknowledges that the United States Government retains a non-exclusive, paid-up, irrevocable, world-wide license to publish or reproduce the published form of this manuscript, or allow others to do so, for United States Government purposes. The Department of Energy will provide public access to these results of federally sponsored research in accordance with the DOE Public Access Plan (<http://energy.gov/downloads/doe-public-access-plan>).

\* Corresponding author at: College of Materials Science and Engineering, Hunan University, Changsha 410082, China.

\*\* Corresponding author at: Department of Nuclear Engineering, University of Tennessee, Knoxville, TN 37996, USA.

E-mail addresses: [tyang7@utk.edu](mailto:tyang7@utk.edu) (T. Yang), [szinkle@utk.edu](mailto:szinkle@utk.edu) (S.J. Zinkle).

cubic) lattices. This suppresses some of the phase instability disadvantages of conventional multi-component concentrated alloys, and therefore HEAs can exhibit many attractive mechanical properties, such as excellent low temperature fracture-resistance [9,10], strong resistance to softening (high strength and low plasticity) at high temperatures [11,12], high hardness [13], encouraging fatigue resistance [14] and wear resistance [15]. Furthermore, HEAs encompass a large family of alloys, and thus a wide range of microstructures and mechanical properties can be achieved by adjusting the compositions of HEAs, which substantially extends the potential applications of HEAs.

Due to their unique structures and excellent mechanical properties, HEAs have been proposed as promising candidates for structural applications in advanced nuclear energy systems [6]. Many investigations have studied the irradiation responses of HEAs [16]. Recent work has shown that the accumulation of irradiation-induced structural damage at room temperature can be suppressed with increasing principal elements [17]. Furthermore, Jin et al. [18] compared the volume swelling of Ni-containing equiatomic alloys under high temperature ion irradiation (500 °C), and found that the volume swelling can be decreased by controlling the number and the type of alloying elements. FeCoCrMnNi HEA showed the lowest volume swelling (<0.2%) after irradiation to ~53 displacement per atom (dpa) at 500 °C, which was 30 times lower than Ni (~6.7%) [18]. These results are highly encouraging indications that HEAs may be good candidates for nuclear energy systems. Generally, the improved irradiation resistance of HEAs is attributed to the high-level lattice distortions and compositional complexities [17–20].

The defect behavior of as-irradiated HEAs has been investigated to unveil the fundamental controlling mechanisms on irradiation tolerance of HEAs. He et al. studied the defect structure of FeCoCrNi irradiated with high energy electrons at 400 °C and found that irradiation-induced defects included elliptical Frank (faulted) loops and polygonal perfect loops [21,22]. Both dislocation loops were interstitial-type and the growth of dislocation loops in FeCoCrNi was 40 times slower than that in pure Ni. Lu et al. compared the irradiation-induced defects in NiFe, NiCoFe, NiCoFeCr and NiCoFeCrMn at 500 °C and also observed faulted 1/3(111) loops and perfect 1/2(110) loops in the as-irradiated alloys [23]. The relative percentage of irradiation-induced faulted loops was found to increase with the number of components, which indicated the evolution and growth of dislocation loops could be suppressed by increasing the compositional complexity. Kiran Kumar et al. studied the microstructure of a Co-free HEA FeNiMnCr under high temperature ion irradiation and found that the FeNiMnCr exhibited a smaller defect cluster size and higher cluster density, as compared with conventional ion-irradiated Fe–Cr–Ni alloys at 400–700 °C [24]. These experimental results suggest that the evolution of irradiation-induced defects can be restrained and delayed by increasing the number of components (compositional complexity) in concentrated solid solution alloys, resulting in the good irradiation tolerance of HEAs.

Although the irradiation responses and defect behavior of HEAs have been preliminarily studied, most investigations were focused on several model HEAs and single-phase concentrated solid-solution alloy (SP-CSA) systems, such as FeCoCrMnNi, FeCoCrNi, NiCoCr, etc., to explore the fundamental mechanisms influencing the defect behavior and irradiation tolerance of HEAs. The irradiation responses of many newly emerging HEAs with attractive mechanical properties have not yet been studied. Moreover, many previous studies were focused on the effects of compositional complexity on the defect behavior of HEAs at a single irradiation temperature; only a limited number of investigations have examined effects of temperature on irradiation-induced defects.

$\text{Al}_x\text{CoCrFeNi}$  is a well-studied HEA system [25–29]; the microstructure and mechanical properties of  $\text{Al}_x\text{CoCrFeNi}$  can be significantly modified by varying the Al concentration due to the large

atomic radius of Al. In the current study, the structural damage and phase stability of initially single phase  $\text{Al}_{0.3}\text{CoCrFeNi}$  irradiated with heavy ions to a peak dose of ~31 dpa at elevated temperatures (250–650 °C) were studied.  $\text{Al}_{0.3}\text{CoCrFeNi}$  was chosen because (i) it is in the compositional boundary region between single phase and multi-phase in the phase diagram, thereby serving as a good model system to study the phase stability of HEAs under irradiation; (ii) it has very good mechanical properties [29–34], in particular good ductility at room temperature and high strength at high temperatures [35], which are important for applications in advanced nuclear energy systems. The irradiation effects were characterized by transmission electron microscopy (TEM) and atom probe tomography (APT), focusing on the evolution of irradiation-induced defects with temperature and phase stability of  $\text{Al}_{0.3}\text{CoCrFeNi}$  under high temperature irradiations.

## 2. Experimental

The  $\text{Al}_{0.3}\text{CoCrFeNi}$  alloy was prepared by vacuum-levitation, melting a mixture of pure metals Al, Co, Cr, Fe and Ni in a high-purity argon atmosphere. The source materials had a purity level higher than 99.0 wt percent (wt.%). The ingots were remelted at least three times in order to promote chemical homogeneity. The as-fabricated  $\text{Al}_{0.3}\text{CoCrFeNi}$  samples were characterized by X-ray diffraction (XRD), scanning electron microscopy (SEM) equipped with an electron back-scattered diffraction (EBSD) detector, APT and TEM.

All samples were mechanically polished using fine metallographic abrasive paper and diamond paste. The polished samples were irradiated with 3 MeV Au ions to a fluence of  $6 \times 10^{15} \text{ cm}^{-2}$  (~31 dpa at damage peak) at four different temperatures: 250 °C, 350 °C, 500 °C and 650 °C [36,37]. The corresponding defect production and stopping range in samples were calculated using SRIM 2013 assuming a displacement threshold energy of 40 eV in the quick Kinchin-Pease option [38]. The damage (dpa) and implanted ion concentration profiles are shown in Fig. S1 in the Supplementary Information.

Cross-sectional TEM samples were all prepared by mechanical polishing, followed by ion milling to form a wedge with sufficient electron transparency. TEM observations were conducted using a 300 keV, Tecnai F30 microscope. The foil thickness was measured by an electron energy loss spectroscopy (EELS) system equipped on the TEM. APT measurements were conducted using a local electrode atom probe (CAMECA LEAP 4000X HR) with a 50 pJ laser energy, a pulse repetition rate of 200 kHz, a 30 K base temperature, and a 0.5% detection rate. A dual beam FIB-SEM system (FEI Nova 200) was used to prepare the needle-shaped APT tips following procedures described elsewhere [39,40]. A Ni film with thickness of ~60 nm was deposited on all samples using a South Bay Technologies Ion Beam Deposition system (IBSe) to protect the surface before sample preparation.

## 3. Results

### 3.1. Microstructure of as-fabricated $\text{Al}_{0.3}\text{CoCrFeNi}$ sample

Fig. 1(a) shows the representative EBSD image of an as-fabricated  $\text{Al}_{0.3}\text{CoCrFeNi}$  sample. Several large grains (with some embedded twins) are visible with grain sizes ranging from hundreds of  $\mu\text{m}$  to a millimeter. All the diffraction peaks in the XRD spectrum of the as-fabricated alloy (as shown in Fig. 1(b)) can be indexed as a FCC crystal structure with a lattice constant of 3.585 Å. Bright field (BF) TEM imaging and corresponding selected area electron diffraction (SAED) analysis (as shown in Fig. 1(c) and 1(d)) confirmed the as-fabricated  $\text{Al}_{0.3}\text{CoCrFeNi}$  to be single FCC phase with a large grain size, and no observable precipitates.

The composition and elemental solute spatial distributions in the as-fabricated sample were characterized by APT, as shown in Fig. 2.

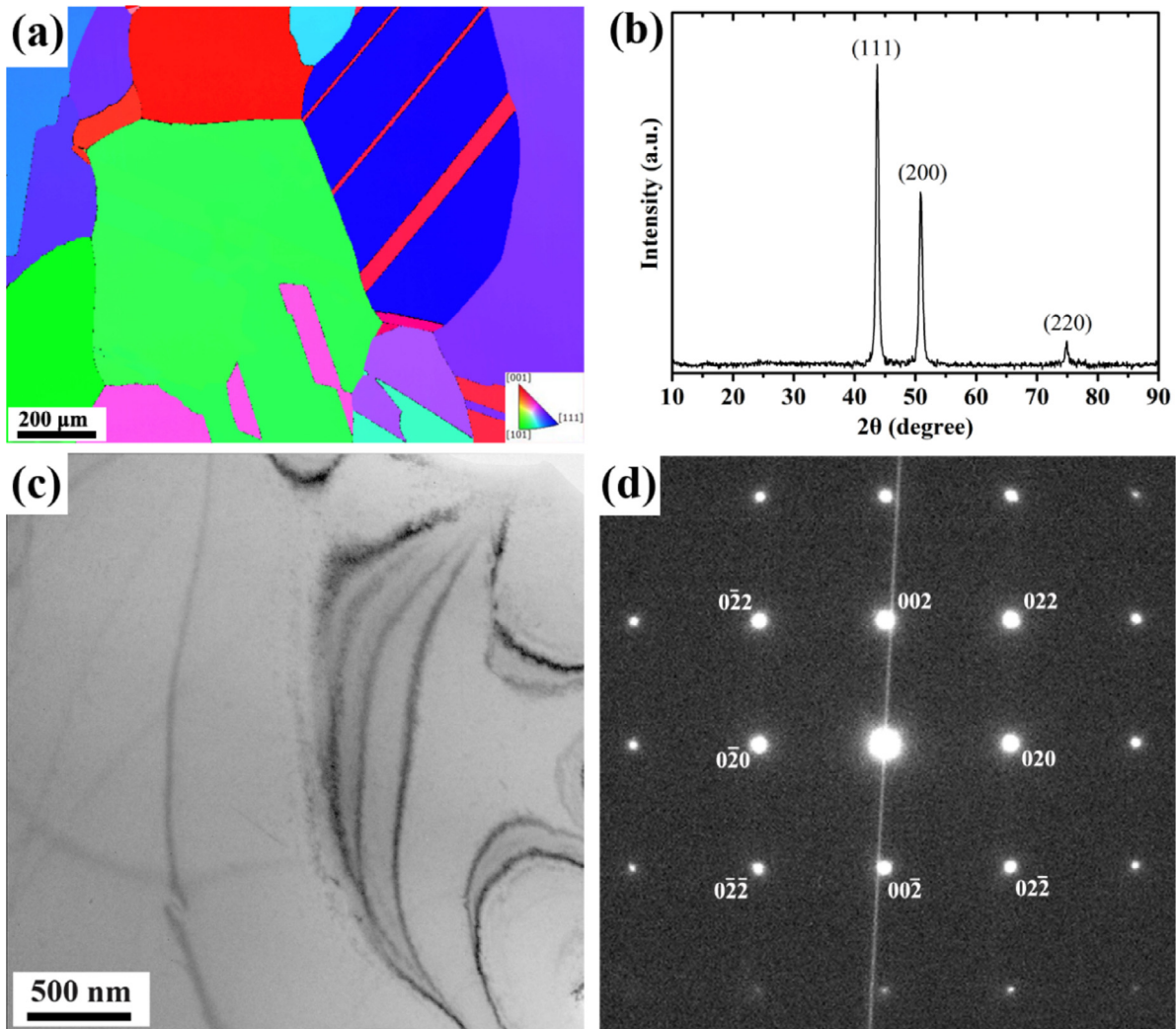


**Fig. 1.** Microstructure of as-fabricated  $\text{Al}_{0.3}\text{CoCrFeNi}$  sample; (a) EBSD image; (b) XRD pattern; (c) BF TEM image; and (d) selected area electron diffraction pattern (SAED) taken from the [100] direction.

The measured composition (at.%) was Al: ~7.0; Co: ~22.4; Cr: ~22.5; Fe: ~23.3; Ni: ~24.3, and the elemental distributions homogeneity was tested using a frequency distribution analysis (FDA). A FDA was performed on a  $15 \text{ nm} \times 15 \text{ nm} \times 15 \text{ nm}$  volume away from poles in the atom probe dataset (as shown in Fig. 2(b–e)), which found no evidence of possible local chemical ordering for Al, Fe, Co and Cr; however, Ni showed a slightly heterogeneous behavior. Ni clustering or precipitation was unable to be visually distinguished in the atom maps or with isoconcentration surfaces, but there was some heterogeneity associated with the poles.

### 3.2. TEM results of $\text{Al}_{0.3}\text{CoCrFeNi}$ irradiated at elevated temperatures

Fig. 3 shows the BF TEM cross section images of  $\text{Al}_{0.3}\text{CoCrFeNi}$  irradiated at four different temperatures, with the original surface located at the top of each image. All BF images in Fig. 3 were taken under two-beam BF conditions using a diffraction vector  $g = (0\bar{2}2)$  near the [211] zone axis. The irradiation-induced structural damage and its evolution with temperature can be clearly observed. At lower temperatures ( $250^\circ\text{C}$  and  $350^\circ\text{C}$ ), a highly damaged region containing a high density of small defect clusters was present over the depth range of  $300\text{--}700\text{ nm}$  (as shown in Fig. 3(a and b)). Detailed characterization using a diffraction vector  $g = (002)$  near the [110] zone axis revealed two groups of edge-on dislocation loops with an intersection angle of  $71^\circ$  in the highly damaged region (as shown in Fig. 4(a

and b)). This intersection angle and orientation with respect to the crystal direction are consistent with {111} habit planes. The average sizes of dislocation loops in the samples irradiated at  $250^\circ\text{C}$  and  $350^\circ\text{C}$  are similar, with diameters of  $12.8\text{ nm}$  and  $14.1\text{ nm}$ , respectively (as shown in Fig. 5(a)), and the corresponding loop densities are  $1.8 \times 10^{22} \text{ m}^{-3}$  and  $1.6 \times 10^{22} \text{ m}^{-3}$ , respectively (as shown in Fig. 5(b)). Besides the dislocation loops, some small defect clusters and small dislocation segments were also observed in the highly damaged region and near surface region, respectively. Most of these small defect clusters appeared as black dots smaller than  $\sim 5\text{ nm}$ . Based on previous results of irradiation-induced structural damage in SP-CSAs [17,41,42] and high magnification observations reported later in this paper, these defects are predominantly small stacking-fault tetrahedra (SFTs).

As the irradiation temperature increased to  $500^\circ\text{C}$  (as shown in Fig. 3(c)), the highly damaged region disappeared. Instead, a moderate density of large and isolated defect clusters was observed in this region. The average size of dislocation loops increased to  $32.7\text{ nm}$  (as shown in Fig. 5(a)), while the loop density decreased to  $3.0 \times 10^{21} \text{ m}^{-3}$  (as shown in Fig. 5(b)).

Weak beam dark field (WBDF) imaging and the “ $g \cdot b$ ” method were employed to obtain a more detailed characterization of the dislocation loops in the  $500^\circ\text{C}$  irradiated sample. Figs. 6 and 7 exhibit the WBDF images of nearly edge-on (Fig. 6) and nearly face-on dislocation loops (Fig. 7), which were taken with  $g = (00\bar{2})$  and  $g = (002)$

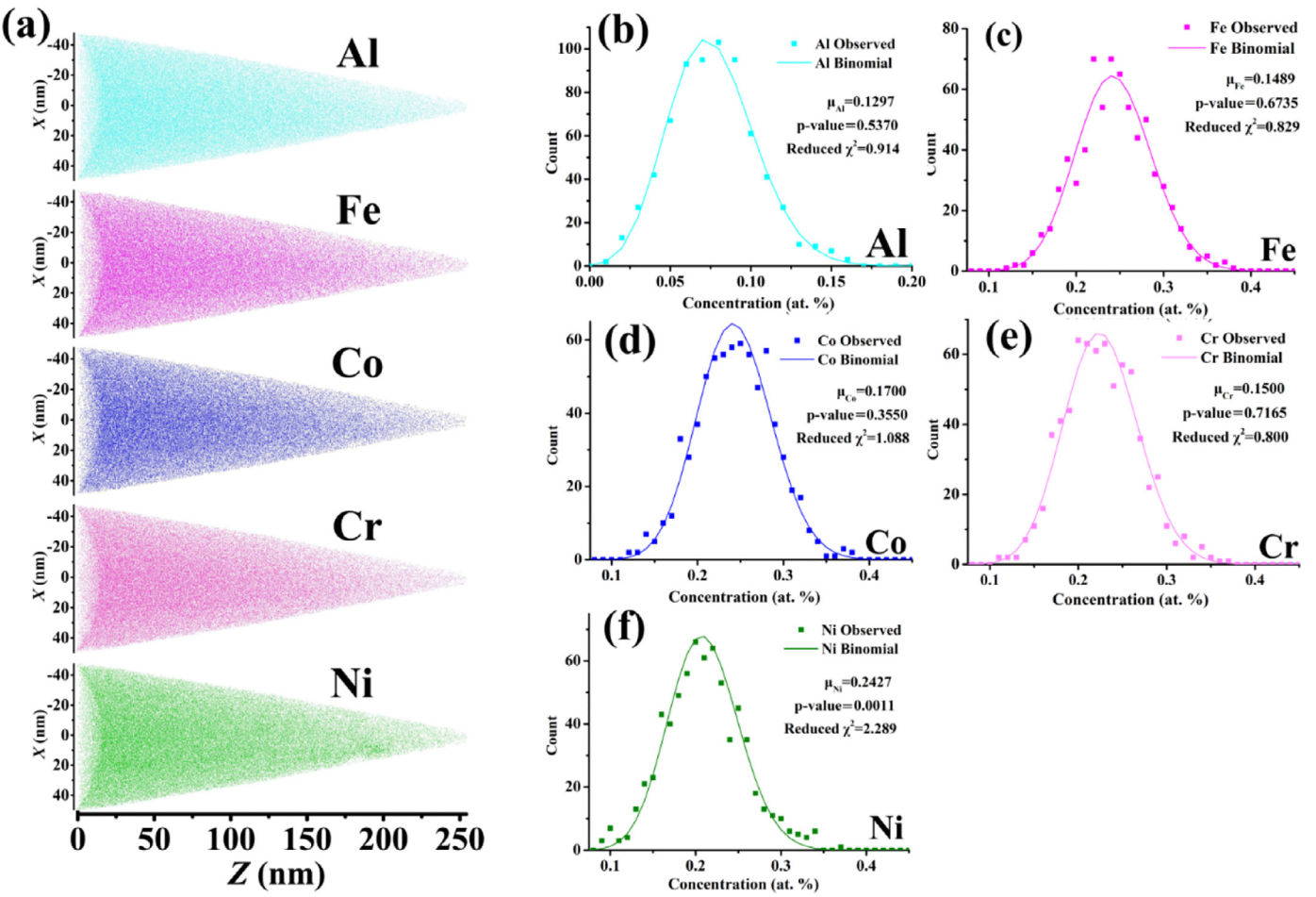


Fig. 2. (a) The atom maps of Al, Fe, Co, Cr, Ni for as-fabricated  $\text{Al}_{0.3}\text{CoCrFeNi}$  sample; (b)–(f) the frequency distribution analyses of the atom probe dataset.

near the [110] zone axis, respectively. The fringes inside the loop periphery, which are characteristic of faulted dislocation loops for this diffraction vector, can be clearly observed, demonstrating that many of these defects are faulted loops. The “ $g \cdot b$ ” analysis revealed (as shown in Fig. S2 in Supplementary Information) the Burgers vectors of the five nearly face-on dislocation loops visible in Fig. 7 were  $b = \pm 1/3 [111]$ . Based on characterization results of WBDF imaging and dislocation loop observation of ion-irradiated FCC alloys [23,43], these defects, including nearly edge-on and face-on dislocation loops, were determined to be faulted  $1/3\langle 111 \rangle$  edge-type dislocation loops lying on  $\{111\}$  habit planes. The edge-on dislocation loops were located on  $(\bar{1}\bar{1}1)$  and  $(\bar{1}1\bar{1})$  planes, indicated by red arrows and blue arrows in Fig. 6(a and b), respectively; while the face-on dislocation loops were located on  $(111)$  plane. The relative orientations of electron beam,  $g$  vectors and habit planes of faulted loops are illustrated in Figs. 6(c and d) and 7(c), respectively.

Based on the conventional inside-outside method using  $\pm g$  (as shown in Figs. 6 and 7), it was found that the faulted dislocation loops in the 500 °C irradiated specimen were all interstitial-type. Since the defect distribution and morphologies are qualitatively similar for the lower irradiation temperatures, it is reasonable to believe that the dislocation loops formed at 250 °C and 350 °C are also interstitial-type  $1/3\langle 111 \rangle$  faulted loops.

Near the peak damage region (400–700 nm) of the 500 °C irradiated specimen, most of irradiation-induced defects are faulted  $1/3\langle 111 \rangle$  loops, as shown in Fig. 4(c), and Fig. S3–S4 in Supplementary Information. Some triangle-shaped SFTs were also observed in this region, as shown in the inset of Fig. 4(c) and Fig. 8. Numerous dislocation segments and perfect loops were

observed in the near surface region (0–400 nm, as shown in Fig. 9); the corresponding density and percentage of perfect loops is  $\sim 1.5 \times 10^{21} \text{ m}^{-3}$  and  $\sim 50\%$  over the entire irradiated region. Lu et al. [23] studied the fraction of faulted loops in ion irradiated NiFe, NiCoFe, NiCoFeCr and NiCoFeCrMn (3 MeV Ni,  $5 \times 10^{16} \text{ cm}^{-2}$ , 500 °C), and found the fraction of faulted loops in NiCoFeCr and NiCoFeCrMn were  $\sim 65\%$  and  $\sim 50\%$ , which are basically consistent with current study if different irradiation ions and fluences are considered. It should be noted that the observed depth range of irradiation-induced structural damage at 250–500 °C ( $\sim 700$  nm) exceeded the depth range predicted by SRIM ( $\sim 500$  nm, Fig. S1 in the Supplementary Information). A similar observation of displacement damage beyond the SRIM predicted damage depths has been reported in other ion-irradiated materials, such as Ni, NiFe and NiCo, and has been attributed to mobile defect diffusion beyond the irradiated region [20].

At the highest irradiation temperature of 650 °C, BF imaging (as shown in Fig. 3(d)) shows a dramatic decrease in the defect cluster density; only long dislocation lines and networks were observed. No faulted loops could be found in the TEM image using a diffraction vector  $g = (002)$  near the [110] zone axis (as shown in Fig. 4(d)), which suggests that the dislocation loops have grown and intersected each other to produce a network dislocation structure, as is commonly observed in conventional FCC materials at elevated irradiation temperatures [43–45]. From similar irradiation studies on other FCC materials, the small vacancy-type defect clusters were expected to become thermally unstable at high temperatures such 650 °C and might dissociate or transform to other defects. As compared to lower temperatures (250–500 °C), the 650 °C damaged region containing

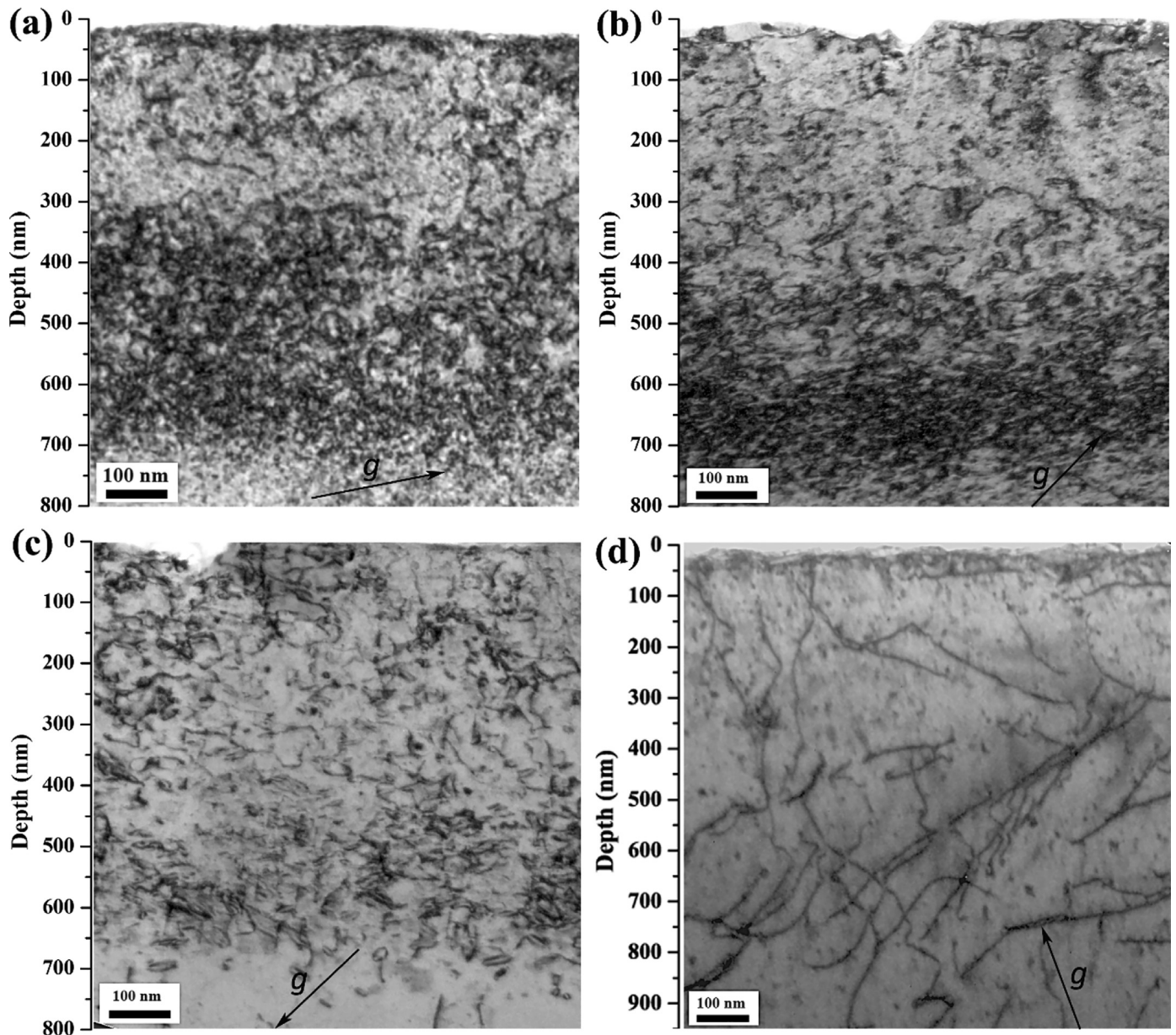


**Fig. 3.** BF images of  $\text{Al}_{0.3}\text{CoCrFeNi}$  irradiated with 3 MeV Au ions to  $6 \times 10^{15} \text{ cm}^{-2}$  at (a) 250 °C; (b) 350 °C; (c) 500 °C; and (d) 650 °C, respectively. Note that the depth range of (d) is larger than that of others. All BF images were taken under two-beam BF conditions using a diffraction vector  $g = (\bar{0}2\bar{2})$  near the [211] zone axis.

long dislocation segments extended toward deeper regions as far as  $\sim 1 \mu\text{m}$  from the surface.

### 3.3. Phase stability of $\text{Al}_{0.3}\text{CoCrFeNi}$ irradiated at elevated temperatures

The as-fabricated alloy consists of a homogeneous elemental distribution as shown by the TEM and APT results in Figs. 1 and 2. To study the phase stability of  $\text{Al}_{0.3}\text{CoCrFeNi}$  under high temperature ion irradiations, including the possible compositional fluctuation, precipitation, decomposition and phase transformation, the microstructures of the irradiated region were characterized by APT and TEM. The underlying unirradiated region (which experienced the same heating process as the irradiated regions without any irradiation), was also characterized to clarify the effects of thermal annealing at various temperatures.

Figs. 10 and 11 show the SAED patterns and high-resolution TEM (HRTEM) images combined with the Fast Fourier Transformation (FFT) images, respectively, of the unirradiated region and irradiated

regions for  $\text{Al}_{0.3}\text{CoCrFeNi}$  irradiated at 250–650 °C. It can be seen that the  $\text{Al}_{0.3}\text{CoCrFeNi}$  FCC solid solution phase was stable for temperatures below 500 °C in both irradiated and unirradiated regions. Only diffraction spots belonging to the FCC phase were observed in both the irradiated region and unirradiated region (Fig. 10(a and b) and (e and f)), and no precipitates were observable in the HRTEM images (as shown in Fig. 11(a and b) and (e and f)).

However, the unirradiated region and irradiated region exhibited opposite precipitation behavior at 500 °C and 650 °C. Coherent superlattice diffractions spots associated with the L1<sub>2</sub> precipitate structure were present in the SAED patterns of the unirradiated region at 500 °C, as shown in Fig. 10(c). The FFT of the HRTEM image also confirmed the formation of coherent L1<sub>2</sub> precipitates in the unirradiated region (as shown in the inset of Fig. 11(c)), and the inverse FFT image (Fig. 12(a)) revealed the average size of the L1<sub>2</sub> precipitates to be about 2–5 nm. When the irradiation temperature was further increased to 650 °C, the superlattice spots of L1<sub>2</sub> became nearly invisible in the SAED pattern of the unirradiated region, indicating the L1<sub>2</sub> structure was thermally

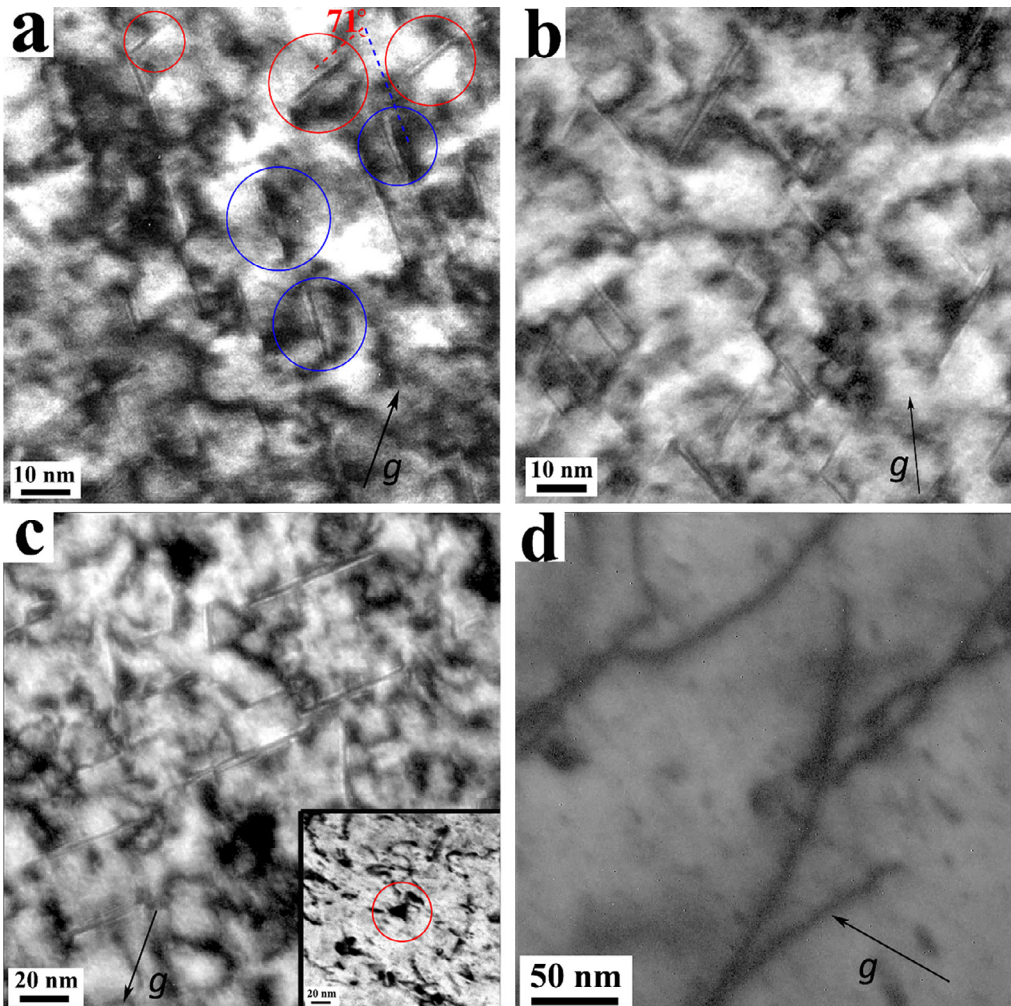


**Fig. 4.** BF TEM images taken with a diffraction vector  $g = (002)$  near the [110] zone axis showing the defect structures of  $\text{Al}_{0.3}\text{CoCrFeNi}$  irradiated at (a) 250 °C; (b) 350 °C; (c) 500 °C and (d) 650 °C. Edge-on dislocation loops on {111} habit planes can be observed at 250 °C, 350 °C and 500 °C. The inset of (c) shows a typical stacking-fault tetrahedron (indicated by the red circle). Note that the scale bars are different due to the different defect sizes. (For interpretation of the references to colour in this figure legend, the reader is referred to the web version of this article.)

unstable at 650 °C. In contrast to the unirradiated region, the SAED patterns and HRTEM images show that the irradiated region maintained the single FCC phase with no evidence of precipitates for an irradiation temperature of 500 °C (as shown in Figs. 10(g) and 11(g)). This indicates that irradiation with 3 MeV Au ions can suppress the thermally-

enhanced or -induced precipitation in  $\text{Al}_{0.3}\text{CoCrFeNi}$  at 500 °C. Conversely, weak but distinct superlattice diffraction spots of B2 structure were observed in the SAED pattern of the irradiated region at 650 °C, as shown in Fig. 10(h). The FFT of the HRTEM image also confirmed the formation of B2 structure precipitates (as shown in the inset of

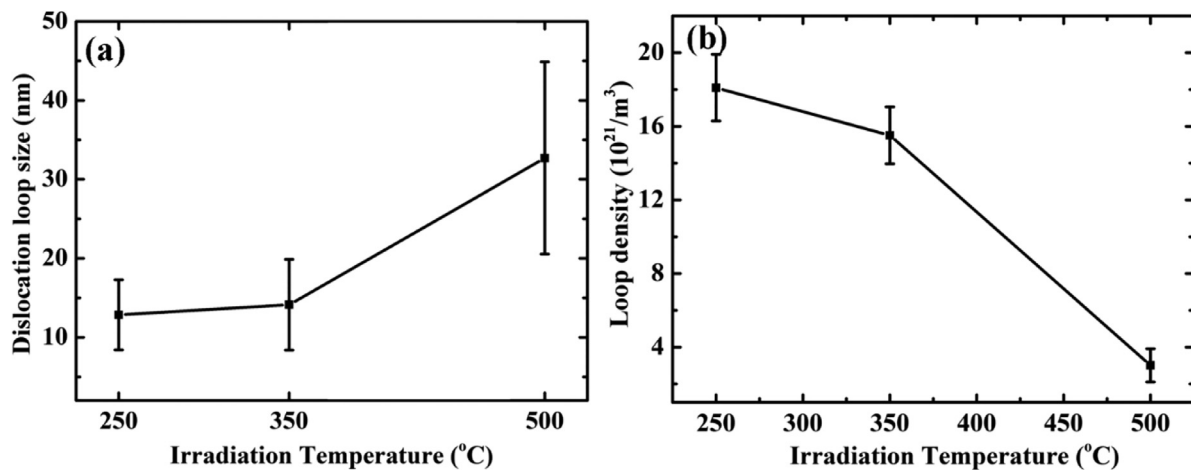


**Fig. 5.** (a) Average size and (b) density of dislocation loops for  $\text{Al}_{0.3}\text{CoCrFeNi}$  irradiated at different temperatures.

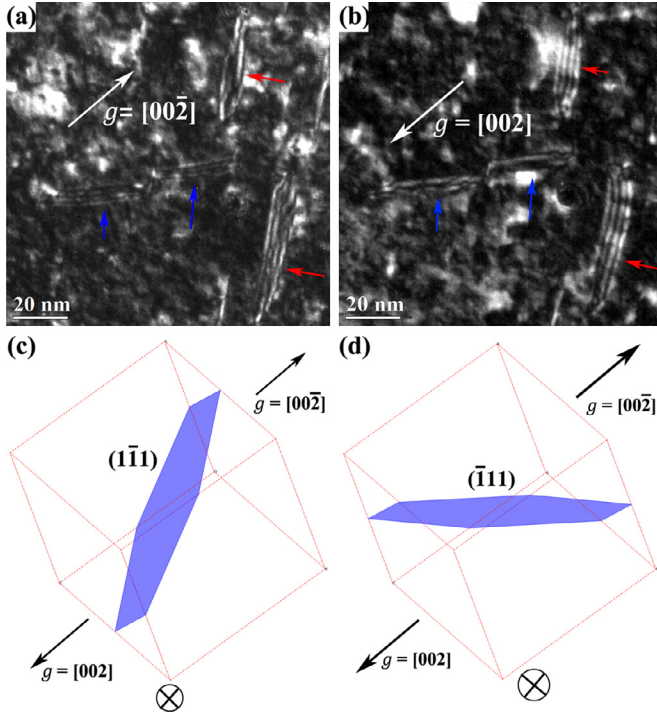


**Fig. 6.** (a) and (b) exhibit the (g, 3 g) WBDF images of four representative dislocation loops on (111) and ( $\bar{1}\bar{1}1$ ) planes, respectively, which were taken with (a)  $g = (00\bar{2})$  and (b)  $g = (002)$  near [110] zone axis; (c) and (d) illustrate the orientations of dislocation loops and directions of g vectors and electron beam, respectively.

Fig. 11(h)), and the inverse FFT image in Fig. 12(b) revealed the average size of the B2 precipitates was 6–10 nm, which was larger than that of the L12 precipitates formed in the unirradiated region at 500 °C.

Since Ni and Al can form several intermetallic compounds with L12 and B2 structures, it was expected that these precipitates might be enriched with Ni and Al. Fig. 13 shows APT reconstructions with Au ions (yellow) and 29 at.% Ni isoconcentration surfaces (green surfaces) of  $\text{Al}_{0.3}\text{CoCrFeNi}$  irradiated at different temperatures. The APT results revealed that a large number of nano precipitates were homogeneously present in the unirradiated regions (> 500 nm depth) and the precipitate density and size were obviously increased with increasing irradiation temperature from 250 °C to 500 °C. Conversely, Ni-rich precipitates were not observed in the unirradiated regions at 650 °C. The proximity histograms of concentration profiles from the matrix to the precipitates are given in Fig. 14. These histograms confirmed that the precipitates were enriched with Ni, Al and depleted in Fe, Co, Cr. The compositional segregation increased with temperature, and the concentrations of

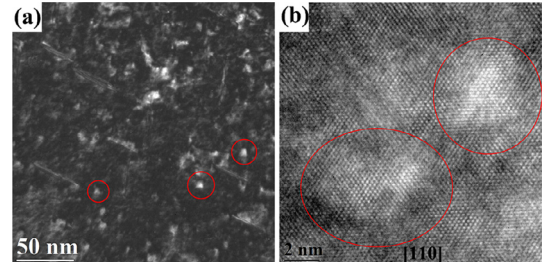


**Fig. 8.** (a) ( $g, 3 g$ ) WBDF TEM image with  $g = \pm [002]$  near [110] zone axis and (b) high resolution TEM image of  $\text{Al}_{0.3}\text{CoCrFeNi}$  irradiated with 3 MeV Au ions at 500 °C. Several defects with the characteristic triangle shape of SFTs are indicated by red circles in (a) and (b). (For interpretation of the references to colour in this figure legend, the reader is referred to the web version of this article.)

Ni and Al in the precipitates increased from ~41 at.% and ~10 at.% to ~55 at.% and ~25 at.%, respectively, when the temperature increased from 250 °C to 500 °C. Note that the precipitates for the 500 °C sample were larger than those in the 250 °C sample. Local magnification effects during an APT experiment, due to differences in evaporation fields between the precipitates and matrix causes ion mixing at the precipitate/matrix interfaces. This effect will cause the precipitate and matrix compositions to mix for smaller precipitates, with the severity of mixing dependent on the precipitate size. Therefore, the real difference of precipitate compositions between different temperatures may be smaller than the measured results.

Compared to unirradiated regions, the irradiated regions have a much lower concentration of detectable precipitation for irradiation temperatures of 250–500 °C. Only a few nano precipitates enriched with Ni and Al were observed in the  $\text{Al}_{0.3}\text{CoCrFeNi}$  irradiated at 350 °C and 500 °C. This is consistent with the TEM results (Figs. 10 and 11) that ion irradiation can suppress the precipitation in  $\text{Al}_{0.3}\text{CoCrFeNi}$  for temperatures below 650 °C. In contrast, several larger precipitates enriched with Ni and Al were present in the irradiated region at 650 °C, while the unirradiated region was nearly precipitate-free (as shown in Fig. 13(d)). The concentrations of Ni and Al solute in detected precipitates were highest (~60 at.% and ~28 at.%, respectively) for the 650 °C irradiated specimen.

APT results confirmed the contrasting precipitation behavior of the unirradiated and ion-irradiated regions of  $\text{Al}_{0.3}\text{CoCrFeNi}$  for the four different irradiation temperatures. Furthermore, irradiation-induced segregation at defects was not observed in the irradiated  $\text{Al}_{0.3}\text{CoCrFeNi}$  at any temperature, which is different from the irradiation responses of  $\text{Al}_{0.1}\text{CoCrFeNi}$  at elevated temperatures [46]. It should be noted that a few Ni-enriched precipitates were observed by APT in the unirradiated regions of  $\text{Al}_{0.3}\text{CoCrFeNi}$  irradiated at 250 °C and 350 °C; however, these small precipitates were not detected by TEM characterization. This was probably attributed to the low density

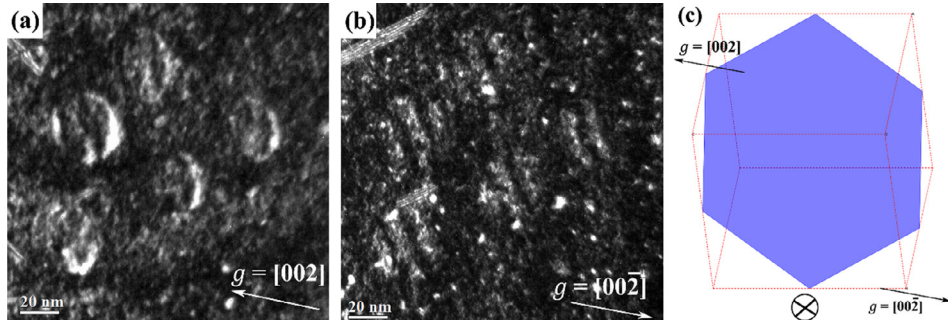


**Fig. 7.** (g, 3 g) WBDF images of five nearly face-on dislocation loops on the (111) plane, which were taken with (a)  $g = (002)$  and (b)  $g = (002\bar{4})$  near [110] zone axis; (c) exhibits the orientations of dislocation loops and directions of g vectors and electron beam, respectively.

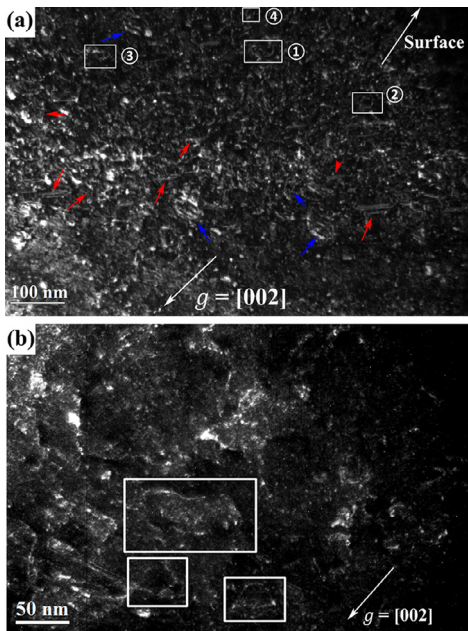


**Fig. 9.** (g, 3 g) WBDF TEM images of  $\text{Al}_{0.3}\text{CoCrFeNi}$  irradiated with 3 MeV Au ions at 500 °C. Both images were taken with  $g = \pm [002]$  near a [110] zone axis. Several nearly edge-on faulted loops and nearly face-on faulted loops in (a) are indicated by red arrows and blue arrows, respectively; the perfect loops are marked by white rectangles and the direction toward surface is also indicated. (b) shows several large perfect loops (outlined by white rectangles) in the near surface region. (For interpretation of the references to colour in this figure legend, the reader is referred to the web version of this article.)

and small size of the precipitates. These precipitates were probably in the incubation period due to the low temperature, and therefore the L12 structure was not completely formed.

#### 4. Discussion

##### 4.1. Irradiation-induced defect evolution at elevated temperatures

Temperature plays an important role in the irradiation-induced structural damage, and the microstructural evolution with irradiation

temperature generally can be divided into five stages according to the defect behavior [43,47,48]. In recovery stage I, only interstitials are capable of long range migration. With increasing temperature, small interstitial clusters and interstitial-impurity complexes start to migrate, corresponding to stage II. In stage III, vacancy motion initiates. Stage IV and V correspond to the migration of vacancy clusters (including vacancy-impurity clusters) and thermal dissociation of sessile vacancy clusters, respectively [43]. When temperature is lower than stage I, defect migration does not occur and the accumulation of irradiation-induced structural damage is typically proportional to the dose until saturation [49]. When the temperature is higher than stage V, irradiation-induced defects typically consists of dislocation loops, network dislocations and voids. SFTs are not stable in this temperature range.

$\text{Al}_{0.3}\text{CoCrFeNi}$  showed a typical temperature-dependent evolution of irradiation-induced defects for FCC metals. As irradiation temperature increased, the defect size increased while the defect density decreased due to the increasing defect mobility and dissociation of small defect clusters. The loop growth and interaction between individual dislocations and loops resulted in the loop unfaulting and formation of perfect  $1/2 \langle 110 \rangle$  loops at 500 °C and the dislocation networks at 650 °C. Similar temperature-dependent effects on the irradiation-induced defects have been observed in many conventional FCC alloys [44–46,48,50–53]. Based on the observed effects of temperature on the irradiated microstructure, the four temperatures in the current study correspond to near or above defect recovery stage III (onset of vacancy migration) to above stage V (thermal dissolution of SFTs and other small vacancy clusters) for  $\text{Al}_{0.3}\text{CoCrFeNi}$  [54].

At 250 °C and 350 °C, numerous interstitial-type dislocation loops can be found up to ~200 nm beyond the damaged region calculated by SRIM, which demonstrates that the interstitial-type defects are mobile and can diffuse beyond the irradiation region. On the other hand, visible vacancy-type defect clusters only include very tiny SFTs. This suggests that both the temperatures 250 °C and 350 °C lie within defect recovery Stage III to IV for  $\text{Al}_{0.3}\text{CoCrFeNi}$ , wherein interstitials and interstitial-type defect clusters have sufficient mobility to migrate and form dislocation loops whereas the irradiation-induced vacancies are predominantly tied up in sessile SFT vacancy clusters that are thermally stable [54]. Similar to prior work on conventional FCC metals [43], recent MD simulations and Cs-corrected STEM indicate that SFTs with sizes of several nm can directly form by the aggregation of vacancies during the picosecond-scale formation and

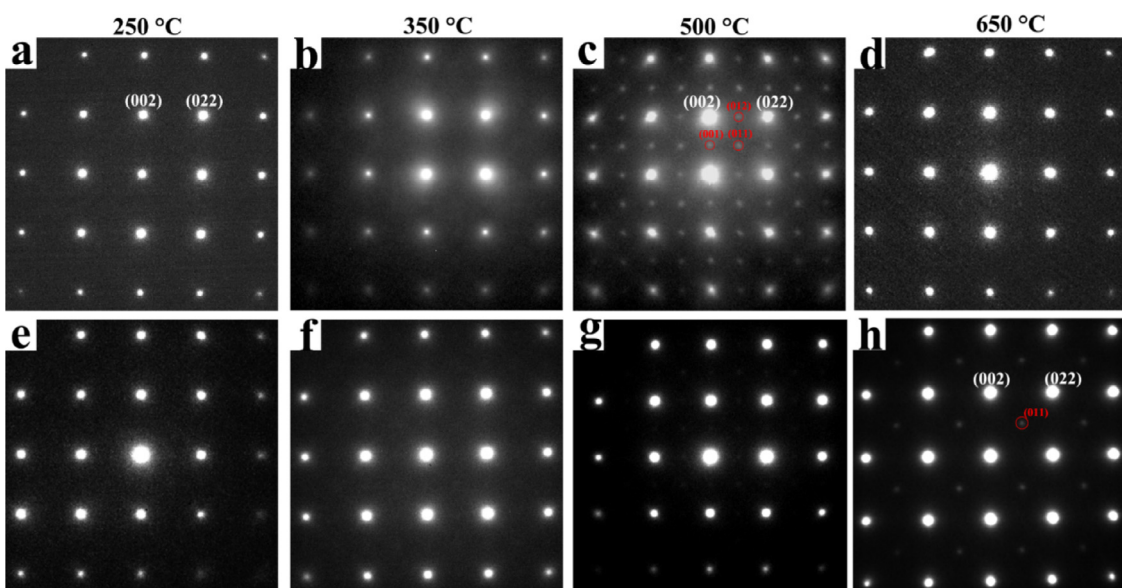


**Fig. 10.** SAED patterns of (a)–(d) unirradiated region and (e)–(h) irradiated region of  $\text{Al}_{0.3}\text{CoCrFeNi}$  at different temperatures. The corresponding irradiation temperatures are 250 °C (a and e), 350 °C (b and f), 500 °C (c and g), 650 °C (d and h), respectively.

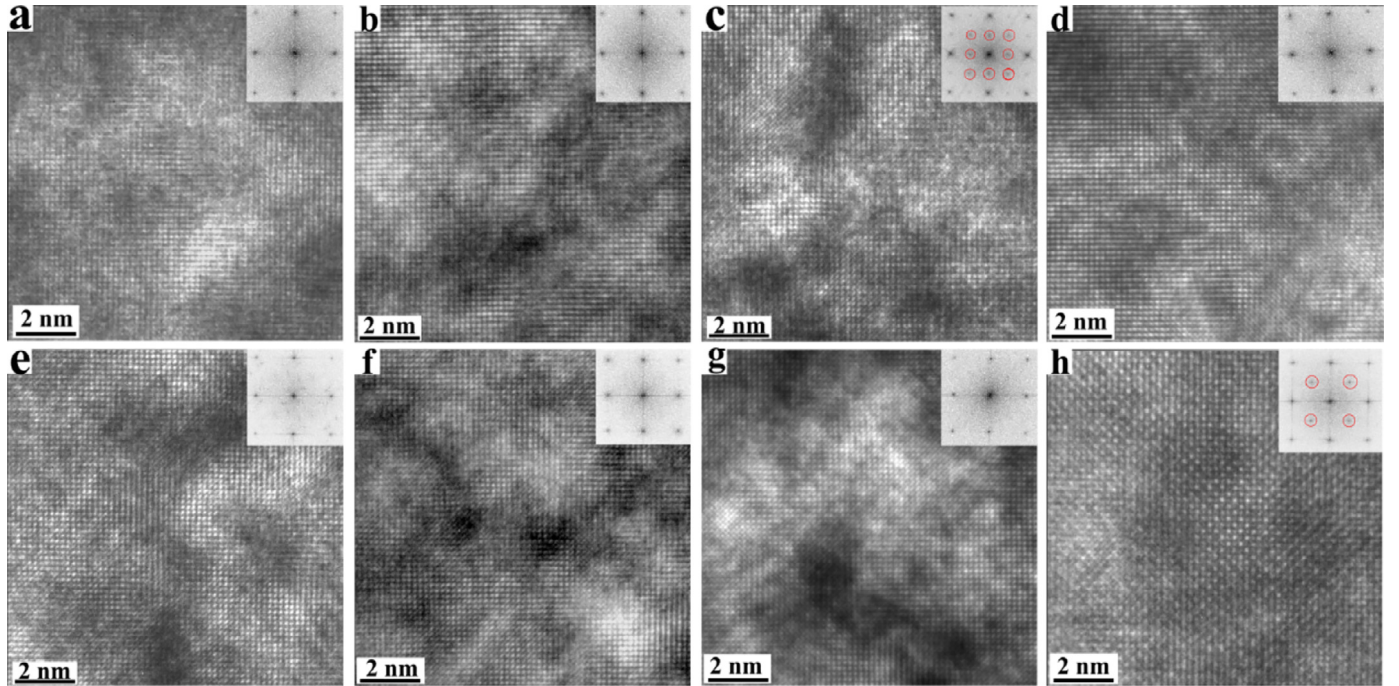


**Fig. 11.** HRTEM images and corresponding FFTs of (a)–(d) unirradiated region and (e)–(h) irradiated region of  $\text{Al}_{0.3}\text{CoCrFeNi}$  at different temperatures. The corresponding irradiation temperatures are 250 °C (a and e), 350 °C (b and f), 500 °C (c and g), 650 °C (d and h), respectively. The superlattice reflections belonging to L12 and B2 in (c) and (h) are marked by red circles in the inset diffraction patterns. (For interpretation of the references to colour in this figure legend, the reader is referred to the web version of this article.)

quenching of displacement cascades in SP-CSAs [19,20,55]. Therefore, most of vacancy-type defects are tiny vacancy clusters and SFTs in this temperature regime, and most of the interstitial-type defects are larger faulted  $1/3\langle 111 \rangle$  dislocation loops on {111} habit planes.

As the irradiation temperature increased to 500 °C, observed irradiation-induced defects became more diverse, including the faulted  $1/3\langle 111 \rangle$  loops, perfect  $1/2\langle 110 \rangle$  loops, dislocation segments and

larger SFTs. This suggests that 500 °C approximately corresponds to recovery stage IV, where the mobility of interstitial clusters is further enhanced and vacancies are highly mobile [43]. In this stage, most of vacancies are still tied up in the SFTs formed in the displacement cascades. Considering the possibility of moderate coarsening of the SFT population during extended irradiation, larger SFTs can be observed compared to the lower irradiation temperatures. Faulted  $1/3\langle 111 \rangle$

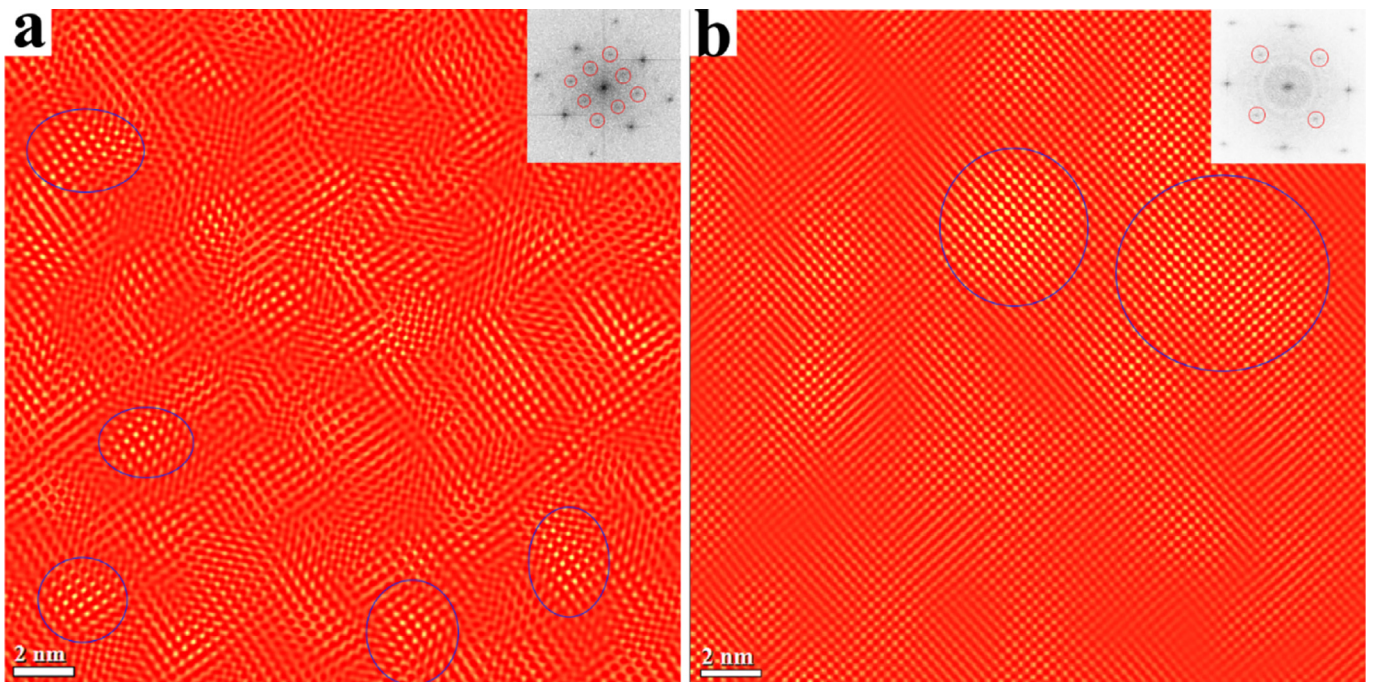


**Fig. 12.** Inverse FFT images of (a) the unirradiated region of  $\text{Al}_{0.3}\text{CoCrFeNi}$  at 500 °C and (b) irradiated region of  $\text{Al}_{0.3}\text{CoCrFeNi}$  at 650 °C. The FFT images were acquired by masking (a) the (010) and (011) reflections of L12 structure and (b) (011) reflections of B2 structure, respectively. Several precipitates with ordered structure are indicated by blue circles. (For interpretation of the references to colour in this figure legend, the reader is referred to the web version of this article.)

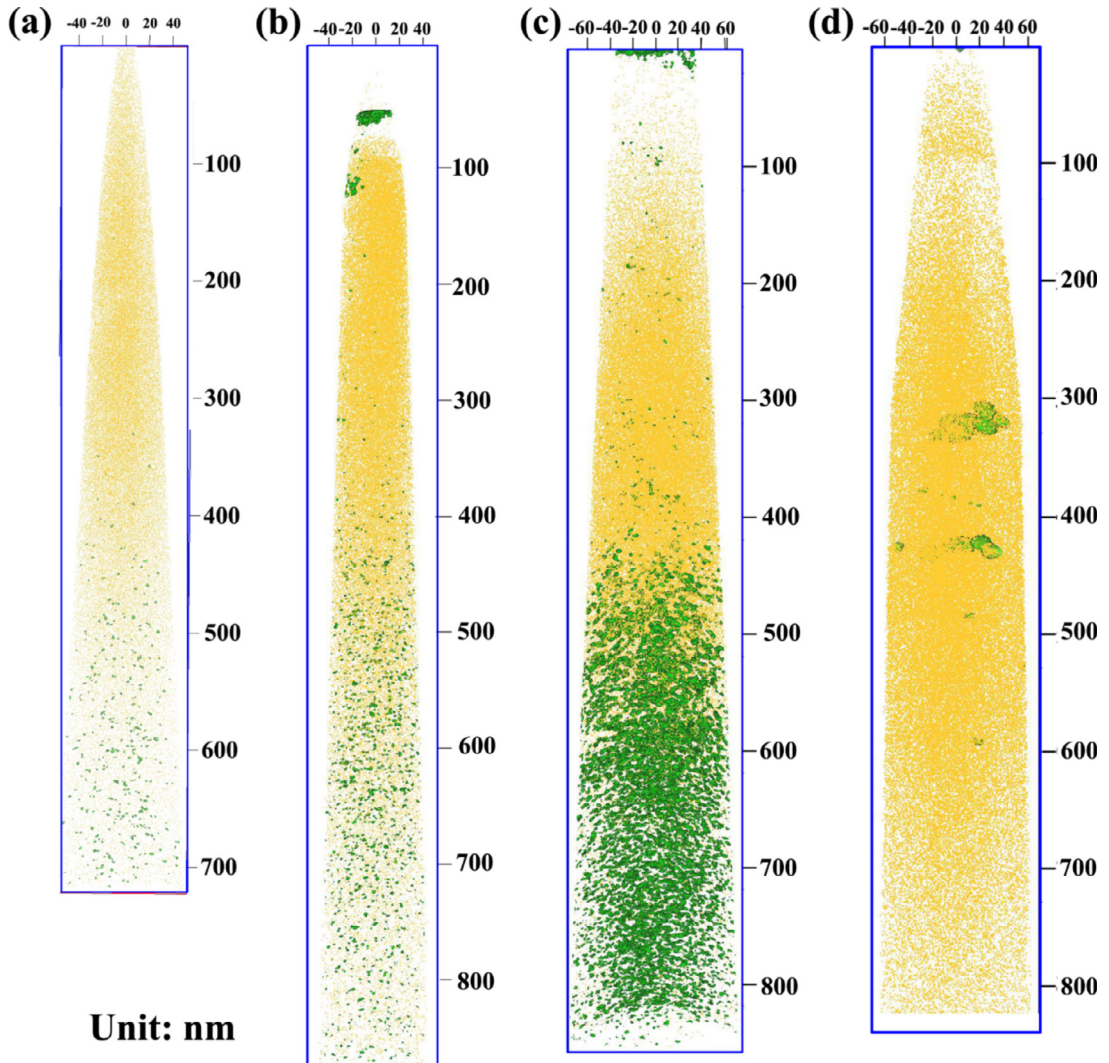


**Fig. 13.** 29 at.% Ni isoconcentration surfaces of  $\text{Al}_{0.3}\text{CoCrFeNi}$  irradiated at (a) 250 °C, (b) 350 °C, (c) 500 °C and (d) 650 °C. The deposited Au ions are indicated by yellow color. (For interpretation of the references to colour in this figure legend, the reader is referred to the web version of this article.)

loops are nucleated at a lower density and thereby become relatively larger compared to lower temperature irradiation by absorbing irradiation-produced interstitials. Some loops can unfault according to the well-known reaction in FCC metals (Eq. (1)), resulting in the formation of perfect  $1/2 \langle 110 \rangle$  loops.

$$\frac{1}{3} \langle 111 \rangle + \frac{1}{6} \langle 112 \rangle = \frac{1}{2} \langle 110 \rangle \quad (1)$$

At 650 °C, only long dislocation segments and dislocation networks were present, indicating the vacancy-type SFTs were thermally unstable at this temperature and that the perfect interstitial-type dislocation loops have grown and interacted to produce a dislocation network, as is commonly observed in conventional FCC alloys [44]. This corresponds to temperatures above recovery stage V, where the irradiation-induced defects generally only include network dislocations, cavities and a few dislocation loops. Thermal dissociation of small defect clusters causes the defect density to be significantly decreased while the defect mobility is greatly enhanced. The mobile defects can migrate a long distance before being absorbed by other defect clusters. Therefore, the depth region of irradiation-induced defects was dramatically increased compared with that at lower temperatures.

It is very interesting to note that Lu et al. [23] compared the structural defects in various Ni-based SP-CSAs irradiated at 500 °C and found that the defect size decreased and the defect density increased

with increasing compositional complexity/number of constituent elements. MD simulations also found that smaller-sized and higher number densities of clusters were formed with increasing compositional complexity [19,41], consistent with TEM and Rutherford back-scattering and channeling (RBS/C) results. These evolutions of defect density and morphology with decreasing compositional complexity are qualitatively similar to the evolution of defects in  $\text{Al}_{0.3}\text{CoCrFeNi}$  with increasing irradiation temperature in the current study (as shown in Fig. 15). The evolution of the defect microstructure in  $\text{Al}_{0.3}\text{CoCrFeNi}$  with increasing irradiation temperature can be attributed to increased defect mobility, along the reduced thermal stability of vacancy clusters. The corresponding mechanisms of the effects of compositional complexity on irradiated microstructure evolution in SP-CSAs have similarly been attributed to the modulation of defect migration, which can significantly delay or reduce the formation of large dislocation loops and voids [23,56].

Furthermore, Zaddach et al. studied and compared the stacking fault energies of Ni, FeNi, FeCrNi, FeCoCrNi and FeCoCrMnNi and found that stacking fault energies decrease with the number of components [57]. This suggests a low stacking fault energy may occur in at least some HEAs, which has been also pointed out by many other studies [58–60]. The energetics analysis of interstitial loops in HEAs was also carried out by Wang et al. [61]. They also found that the stacking fault energy decreases with increasing compositional

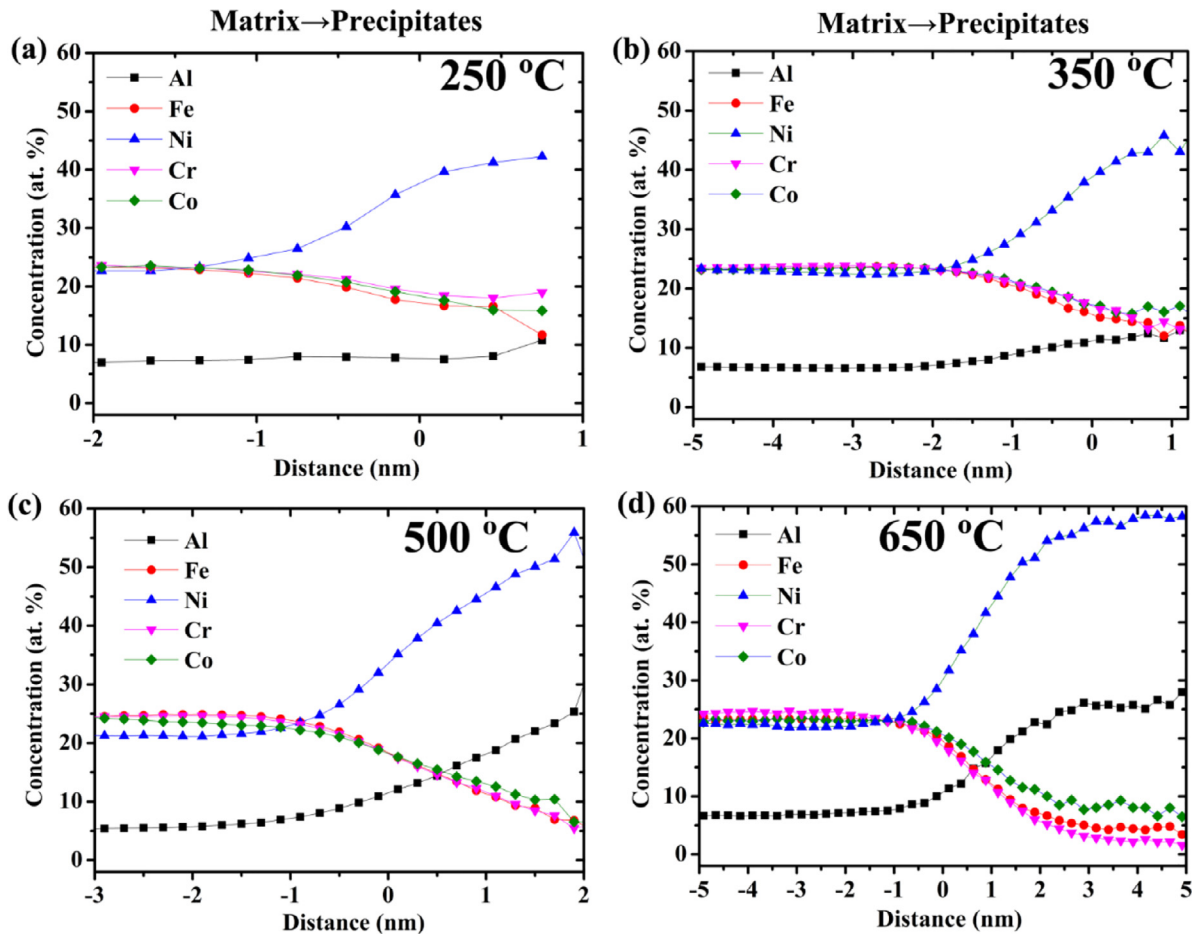


**Fig. 14.** Proximity histograms showing the spatial variations in composition from matrix into precipitates for  $\text{Al}_{0.3}\text{CoCrFeNi}$  irradiated at (a)  $250\text{ }^{\circ}\text{C}$ , (b)  $350\text{ }^{\circ}\text{C}$ , (c)  $500\text{ }^{\circ}\text{C}$  and (d)  $650\text{ }^{\circ}\text{C}$ .

complexity and the low stacking fault energy provides the energetic driving force for the formation of faulted loops in HEAs [61]. Therefore the low stacking fault energy stabilizes the faulted dislocation loops and restrains the transformation from faulted loops to perfect loops. This is consistent with our experiment results ( $\text{Al}_{0.3}\text{CoCrFeNi}$  exhibited a similar but much slower defect evolution with temperature, as compared with conventional FCC alloys) and other studies, such as Lu et al. [23], in which they found that a higher fraction of faulted loops exists in the more compositionally complex alloys, which indicate that increasing compositional complexity can extend the incubation period and delay loop growth. Therefore, the compositional complexity may also restrain the transformation from faulted loops to perfect loops and slow the defect evolution due to a reduction in stacking fault energy.

Based on the qualitatively similar evolution of irradiation-induced defects with temperature and with compositional complexity, an intriguing possibility is that the compositional complexity of multi-component miscible alloy systems can be adjusted to make them favorable for operation in a certain irradiation temperature (tailored irradiation microstructure). Since the defect mobility is low at low temperature, irradiation can produce pronounced hardening due to the formation of a high density of small defect clusters, which serve as obstacles to dislocation motion. In contrast, irradiation induced volume swelling and precipitation/segregation will become significant at higher temperature due to the high defect mobility induced-agglomeration of vacancies and solutes [4]. Nuclear materials are generally used in a temperature window range in which degradation of mechanical properties induced by various deleterious effects is acceptable [62]. Therefore, if we can control the defect mobility by

changing the compositional complexity of SP-CSAs and HEAs in order to avoid the serious hardening or volume swelling for a certain irradiation temperature, this will greatly enhance the flexibility of SP-CSAs and HEAs for use in advanced nuclear energy systems.

Furthermore, a recent study has reported that the stacking fault energy of  $\text{Al}_x\text{CoCrFeNi}$  is increased with increasing Al concentration [63]. Because the evolution of irradiation-induced defects is related to stacking fault energy, the properties of irradiation-induced defects at different temperatures and the microstructural evolution of  $\text{Al}_x\text{CoCrFeNi}$  can potentially be tailored by changing the Al content. This provides a strategy to modify the irradiation responses of  $\text{Al}_x\text{CoCrFeNi}$ , which can promote the application of  $\text{Al}_x\text{CoCrFeNi}$  in advanced nuclear energy systems. However, further investigation is required to further clarify the effects of Al.

It should be noted that no voids were observed in the  $\text{Al}_{0.3}\text{CoCrFeNi}$  irradiated with 3 MeV Au ions at four different temperatures ranging from  $250\text{ }^{\circ}\text{C}$  to  $650\text{ }^{\circ}\text{C}$ . However, voids were observed in many other ion irradiated HEAs and SP-CSAs ( $500\text{ }^{\circ}\text{C}$ , 3 MeV/1.5 MeV Ni), including  $\text{FeCoCrMnNi}$ ,  $\text{FeCoCrNi}$ , etc. [18,56]. The different response to void swelling might be attributed to the effects of deposited ions. It has been pointed out that implanted ions can suppress the formation of voids in numerous metals [64–67]. The maximum depth range of irradiation-induced structural damage of 3 MeV Au ions was predicted by SRIM calculation to be  $\sim 500\text{ nm}$ , while the Au concentration peak of  $\sim 0.4\text{ at.\%}$  occurred at  $\sim 300\text{ nm}$  with a FWHM of  $\sim 200\text{ nm}$  (as shown in Fig. S1 in the Supplementary Information). Therefore the implanted ion effects on void swelling suppression were expected to be significant for 3 MeV Au ions. In contrast, the damage depths of 3 MeV and 1.5 MeV Ni ions were larger, which

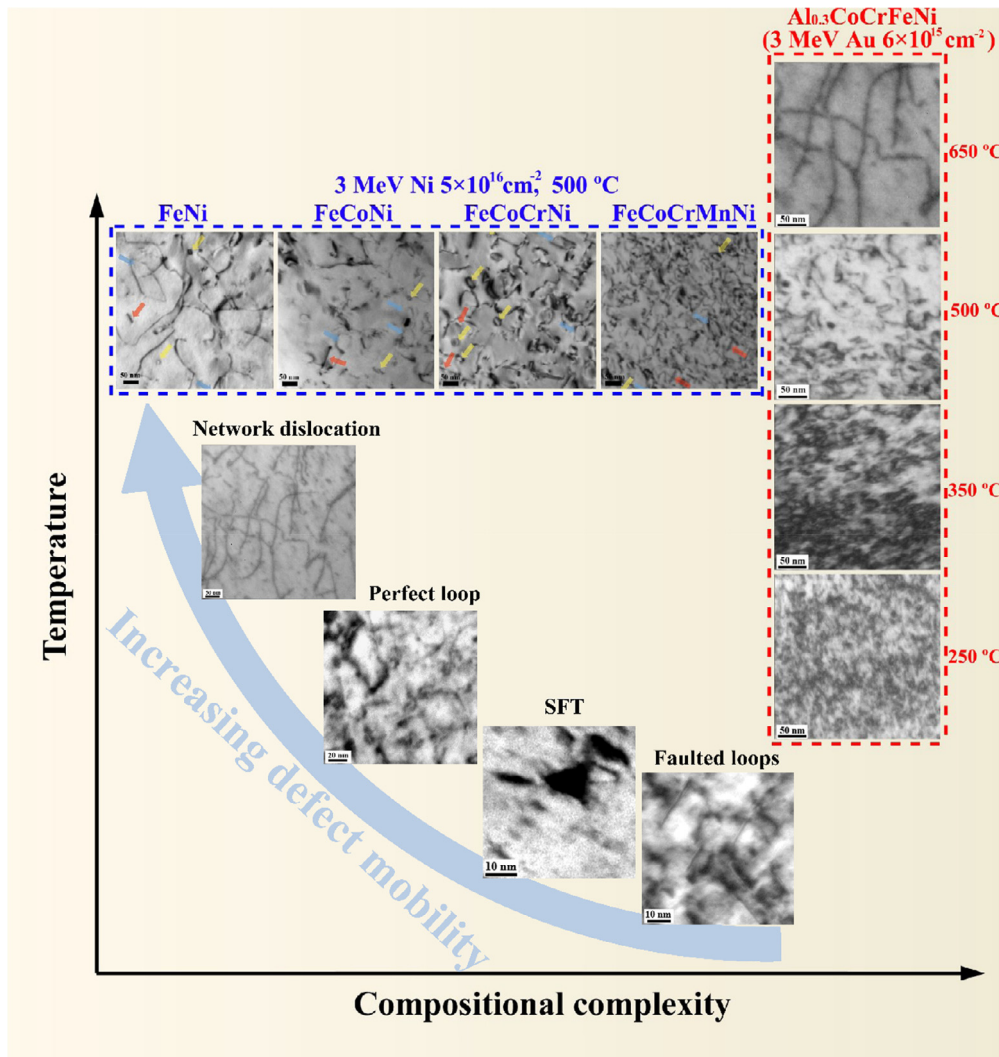


**Fig. 15.** The evolution of irradiation-induced defects with compositional complexity (Ni-based SP-CSAs, 3 MeV Ni, 500 °C) [23] and temperature ( $\text{Al}_{0.3}\text{CoCrFeNi}$ , 3 MeV Au, 250–650 °C), which are outlined by a dashed blue rectangle and red rectangle, respectively. The blue arrow indicates that the defect mobility is increased with increasing temperature and decreasing compositional complexity. (For interpretation of the references to colour in this figure legend, the reader is referred to the web version of this article.)

could reach  $\sim 2 \mu\text{m}$  and  $\sim 1.2 \mu\text{m}$ , respectively. Thus there was a wider safe analysis region [58] for 3 MeV and 1.5 MeV Ni ions, where artifacts associated with effects of the surface and implanted ions were less pronounced. Follow-on ion irradiation studies of the current  $\text{Al}_{0.3}\text{CoCrFeNi}$  HEA using higher energy and/or lower mass bombarding ions would be useful to confirm the void swelling resistance observed in the current investigation.

#### 4.2. Phase stability of $\text{Al}_{0.3}\text{CoCrFeNi}$ irradiated at elevated temperatures

In our previous work, we studied the phase stabilities of Al-containing HEAs with a stable single phase microstructure ( $\text{Al}_{0.1}\text{CoCrFeNi}$ ) and multi-phase microstructure ( $\text{Al}_{0.75}\text{CoCrFeNi}$  and  $\text{Al}_{1.5}\text{CoCrFeNi}$ ) and found that the HEA with a stable single phase microstructure ( $\text{Al}_{0.1}\text{CoCrFeNi}$ ) still retained a homogeneous solid solution structure under irradiation from room temperature to 650 °C [46], but irradiation resulted in the further phase separation for initially multi-phase HEAs even at room temperature [68]. In this work, the phase stability of  $\text{Al}_{0.3}\text{CoCrFeNi}$  under irradiation was different from stable single phase HEA and multi-phase HEAs, which was found to depend on temperature (as shown in Fig. 10). The ion irradiated damage and unirradiated regions also showed opposite precipitation behaviors that changed with increasing irradiation temperature (as shown in Fig. 13).

Gwalani et al. studied the phase stability of  $\text{Al}_{0.3}\text{CoCrFeNi}$  and found the formation of (Ni, Al) enriched L12 precipitates after annealing at 550 °C for 150 h [69]. The L12 precipitates were unstable and replaced by lath-like B2 precipitates after annealing at 700 °C for 50 h and the average size of B2 precipitates (longitudinal axis  $\sim 175 \text{ nm}$ ) was much larger than that of L12 precipitates ( $\sim 5 \text{ nm}$ ) [69]. These prior results on high temperature annealing of  $\text{Al}_{0.3}\text{CoCrFeNi}$  [69] are essentially consistent with the structural evolution of the unirradiated regions at different temperatures in the current study. Numerous small L12 precipitates enriched with Ni and Al were observed in the unirradiated region at 500 °C. When the temperature increased to 650 °C, the small L12 precipitates became unstable and thus the structure nearly became a homogeneous solid solution again. However, no B2 precipitate was found in unirradiated region at 650 °C, which might be a result of the lower temperature (650 °C vs 700 °C) and shorter heating time ( $\sim 3.5 \text{ h}$  vs 50 h) in the current study compared to ref. [69]. B2 precipitates were generally formed in  $\text{Al}_{0.3}\text{CoCrFeNi}$  at longer annealing times or/and higher annealing temperatures [70,71].

Our TEM and APT results revealed that the effects of 3 MeV Au ion irradiation on the precipitation behavior of  $\text{Al}_{0.3}\text{CoCrFeNi}$  varied with increasing temperature. At 500 °C, the irradiation suppressed precipitation of the L12 ordered phase. In contrast, precipitation of the B2 ordered phase was enhanced by irradiation when the temperature

was increased to 650 °C. It should be noted that the precipitation suppression effects of irradiation were also observed at 250 °C and 350 °C (as shown in Fig. 13(a and b)) although only segregation of Ni and Al occurred and the ordered L12 precipitate phase was not fully formed in the unirradiated regions at either temperature.

The phase stability of metastable alloys under ion irradiation has been widely studied by theoretical and experimental methods, especially for immiscible binary alloys [72–80]. Generally, the microstructural evolution depends on the relative importance of two competing dynamical interactions [73]. First, energetic irradiation-induced displacement cascades can induce atomic mixing, resulting in ballistic dissolution of precipitates and the formation of homogeneous solid solution structures. On the other hand, irradiation-enhanced and thermally driven atomic diffusion tends to enhance the nucleation and growth of precipitates if the thermodynamic equilibrium state is a two-phase or multi-phase regime, resulting in the enhanced formation of precipitates in the system. The observed phase stability depends on various factors, including dose rate [75], cascade size, temperature [72], thermodynamic property of alloy system [81], compositional effects [75] and possible coupled solute-defect irradiation induced solute segregation phenomena. Three different steady-state microstructures can be formed [73], including homogeneous solid solution, compositional patterning and macroscopic phase separation, which correspond to an irradiation-induced mixing-dominant system, comparable influences of mixing and diffusion, and thermodynamic diffusion-dominant system, respectively.

It can be expected that the irradiation-induced mixing is dominant in the low temperature region because the thermally driven-atomic diffusion is restrained. Therefore, it is assumed that the irradiation-induced mixing was dominant for  $\text{Al}_{0.3}\text{CoCrFeNi}$  irradiated with 3 MeV Au ions when the temperature was less than or equal to 500 °C, resulting in a homogeneous supersaturated solid solution structure in the irradiated region. It should be noted that although the defect distributions extended to a depth of 700 nm due to defect diffusion, the observed depth range of the solid solution microstructure was only 500 nm, which is consistent with the displacement cascade damaged region calculated by SRIM (as shown in Fig. S1 in the Supplementary Information). This indicates that the precipitation was suppressed by the irradiation induced displacement cascades, instead of subsequent migrating defects. Compared with other binary and ternary FCC alloys [82,83], the temperature range for a pronounced suppression effect of irradiation in  $\text{Al}_{0.3}\text{CoCrFeNi}$  is dominant is very high (> 500 °C), which may be caused by the large displacement cascade size of 3 MeV Au ions and/or sluggish atom diffusion of HEAs [84].

When the irradiation temperature increased to 650 °C, the irradiation by 3 MeV Au ions enhanced the formation and growth of B2 precipitates in the ion irradiated region. Two different mechanisms are proposed to interpret the precipitation enhancement induced by irradiation of 3 MeV Au ions at 650 °C.

First, the precipitation enhancement of  $\text{Al}_{0.3}\text{CoCrFeNi}$  at 650 °C was possibly induced by radiation enhanced diffusion (RED) [85]. A similar effect has been reported in the neutron irradiation embrittlement of reactor pressure vessel (RPV) steel, which is mainly attributed to the irradiation-enhanced precipitation of solutes (Cu, Mn, Ni, Si, P) [86], as well as for numerous other alloy systems. In the current study, it is assumed that the effect of irradiation-induced mixing was less pronounced at 650 °C due to the high thermally driven atomic diffusion and thermodynamic effects dominated the microstructural evolution of the system. Tang et al. [71] compared the annealing-induced phase transformation in nanocrystalline and coarse-grained  $\text{Al}_{0.3}\text{CoCrFeNi}$  HEA and found that the B2 phase was formed in nanocrystalline  $\text{Al}_{0.3}\text{CoCrFeNi}$  HEA at a lower temperature, which was attributed to the enhanced elemental diffusion along grain boundaries in nanocrystalline  $\text{Al}_{0.3}\text{CoCrFeNi}$ . This demonstrates that the increase of atomic diffusion can decrease the threshold temperature of precipitation of B2 phase in  $\text{Al}_{0.3}\text{CoCrFeNi}$  HEA.

Second, the L12 precipitates in the unirradiated region showed a homogeneous distribution. In contrast, the B2 precipitates in the irradiated region at 650 °C exhibited a heterogeneous distribution. The 29 at.% Ni isoconcentration surfaces (green surfaces) of  $\text{Al}_{0.3}\text{CoCrFeNi}$  irradiated at 650 °C were carefully checked in different directions, as shown in Fig. S5 in the Supplementary Information. Combined with the defect morphology revealed by TEM characterization, we speculate the B2 precipitates produced in the 650 °C irradiated region were preferentially formed at dislocation lines. Three groups of precipitates which might be located at different dislocation lines were identified in Fig. S5 in the Supplementary Information. The dislocation lines became nucleation centers, facilitating the formation of B2 precipitates. In contrast, very few dislocations were present in the unirradiated region so heterogeneous nucleation of the B2 phase at 650 °C was suppressed. Moreover the atomic diffusion along dislocation lines was enhanced [87–89], which could also facilitate the precipitation.

## 5. Conclusions

This work studied the irradiation responses of  $\text{Al}_{0.3}\text{CoCrFeNi}$  at elevated temperatures, focusing on the irradiation-induced defects and phase stability. The average size of defect clusters increased while the density decreased with increasing irradiation temperature, and the irradiation-induced dislocation loops transformed from predominantly faulted 1/3(111) dislocation loops at 250 °C and 350 °C to a mixture of faulted 1/3(111) dislocation loops and perfect loops at 500 °C. At the highest irradiation temperature of 650 °C, the stable defects only include long dislocation segments and network dislocations. The evolution of irradiation-induced defects with temperature is similar with many other conventional FCC alloys and can be interpreted by the effects of temperature on the mobilities and thermal stability of interstitials and vacancies and their clusters.

Irradiation by 3 MeV Au ions produced competing effects (due to ballistic mixing and irradiation-enhanced diffusion) on the phase stability at different temperatures. At low temperatures (< 500 °C), irradiation suppressed the precipitation of L12 phases due to the dominant effect of irradiation-induced ballistic mixing at low temperatures. In contrast, irradiation enhanced the precipitation of B2 phases at 650 °C due to the irradiation-enhanced diffusion effects at elevated temperatures. The precipitation of B2 phases was facilitated by RED and irradiation-induced dislocations, which increased the atom mobility and served as nucleation centers for the precipitates, respectively.

## Declaration of competing interest

The authors declare that they have no known competing financial interests or personal relationships that could have appeared to influence the work reported in this paper.

## Acknowledgements

This work was financially supported in part by the Office of Fusion Energy, US Department of Energy (grant # DE-SC0006661 with the University of Tennessee), the National Magnetic Confinement Fusion Energy Research Project 2015GB113000 and the National Natural Science Foundation of China (11905057, 11935004). YZ very much appreciates the financial support from the National Natural Science Foundation of China (Nos. 51671020), 111 Project (B07003), and the Program for Chang-jiang Scholars and the Innovative Research Team of the University. Atom probe tomography was conducted at ORNL's Center for Nanophase Materials Sciences (CNMS), which is a U.S. DOE Office of Science User Facility.

## Supplementary materials

Supplementary material associated with this article can be found in the online version at doi:[10.1016/j.actamat.2020.01.060](https://doi.org/10.1016/j.actamat.2020.01.060).

## References

- [1] S.J. Zinkle, J.T. Busby, Structural materials for fission & fusion energy, *Mater. Today* 12 (11) (2009) 12–19.
- [2] P. Yvon, F. Carré, Structural materials challenges for advanced reactor systems, *J. Nucl. Mater.* 385 (2) (2009) 217–222.
- [3] K.L. Murty, I. Charit, Structural materials for GEN-IV nuclear reactors: challenges and opportunities, *J. Nucl. Mater.* 383 (1) (2008) 189–195.
- [4] S.J. Zinkle, G. Was, Materials challenges in nuclear energy, *Acta Mater.* 61 (3) (2013) 735–758.
- [5] S.J. Zinkle, Advanced materials for fusion technology, *Fusion Eng. Des.* 74 (1) (2005) 31–40.
- [6] S.J. Zinkle, L.L. Snead, Designing radiation resistance in materials for fusion energy, *Annu. Rev. Mater. Res.* 44 (2014) 241–267.
- [7] D.B. Miracle, O.N. Senkov, A critical review of high entropy alloys and related concepts, *Acta Mater.* 122 (2017) 448–511.
- [8] J.W. Yeh, S.K. Chen, S.J. Lin, J.Y. Gan, T.S. Chin, T.T. Shun, C.H. Tsau, S.Y. Chang, Nanostructured high-entropy alloys with multiple principal elements: novel alloy design concepts and outcomes, *Adv. Eng. Mater.* 6 (5) (2004) 299–303.
- [9] B. Gludovatz, A. Hohenwarter, D. Catooor, E.H. Chang, E.P. George, R.O. Ritchie, A fracture-resistant high-entropy alloy for cryogenic applications, *Science* 345 (6201) (2014) 1153–1158.
- [10] B. Gludovatz, A. Hohenwarter, K.V. Thurston, H. Bei, Z. Wu, E.P. George, R.O. Ritchie, Exceptional damage-tolerance of a medium-entropy alloy CrCoNi at cryogenic temperatures, *Nat. Commun.* 7 (2016) 10602.
- [11] O.N. Senkov, G.B. Wilks, D.B. Miracle, C.P. Chuang, P.K. Liaw, Refractory high-entropy alloys, *Intermetallics* 18 (9) (2010) 1758–1765.
- [12] O.N. Senkov, G.B. Wilks, J.M. Scott, D.B. Miracle, Mechanical properties of Nb<sub>25</sub>Mo<sub>25</sub>Ta<sub>25</sub>W<sub>25</sub> and V<sub>20</sub>Nb<sub>20</sub>Mo<sub>20</sub>Ta<sub>20</sub>W<sub>20</sub> refractory high entropy alloys, *Intermetallics* 19 (5) (2011) 698–706.
- [13] P.K. Huang, J.W. Yeh, T.T. Shun, S.K. Chen, Multi-principal-element alloys with improved oxidation and wear resistance for thermal spray coating, *Adv. Eng. Mater.* 6 (1/2) (2004) 74–78.
- [14] M.A. Hemphill, T. Yuan, G.Y. Wang, J.W. Yeh, C.W. Tsai, A. Chuang, P.K. Liaw, Fatigue behavior of Al<sub>0.5</sub>CoCrCuFeNi high entropy alloys, *Acta Mater.* 60 (16) (2012) 5723–5734.
- [15] M.-H. Chuang, M.-H. Tsai, W.-R. Wang, S.-J. Lin, J.-W. Yeh, Microstructure and wear behavior of Al<sub>x</sub>Co<sub>1.5</sub>CrFeNi<sub>1.5</sub>Ti<sub>y</sub> high-entropy alloys, *Acta Mater.* 59 (16) (2011) 6308–6317.
- [16] T. Yang, C. Li, S.J. Zinkle, S. Zhao, H. Bei, Y. Zhang, Irradiation responses and defect behavior of single-phase concentrated solid solution alloys, *J. Mater. Res.* 33 (2018) 3077–3091.
- [17] Y. Zhang, G.M. Stocks, K. Jin, C. Lu, H. Bei, B.C. Sales, L. Wang, L.K. Béland, R.E. Stoller, G.D. Samolyuk, M. Caro, A. Caro, W.J. Weber, Influence of chemical disorder on energy dissipation and defect evolution in concentrated solid solution alloys, *Nat. Commun.* 6 (2015) 8736.
- [18] K. Jin, C. Lu, L.M. Wang, J. Qu, W.J. Weber, Y. Zhang, H. Bei, Effects of compositional complexity on the ion-irradiation induced swelling and hardening in Ni-containing equiatomic alloys, *Scr. Mater.* 119 (2016) 65–70.
- [19] D.S. Aidhy, C. Lu, K. Jin, H. Bei, Y. Zhang, L. Wang, W.J. Weber, Point defect evolution in Ni, NiFe and NiCr alloys from atomistic simulations and irradiation experiments, *Acta Mater.* 99 (2015) 69–76.
- [20] C. Lu, K. Jin, L.K. Béland, F. Zhang, T. Yang, L. Qiao, Y. Zhang, H. Bei, H.M. Christen, R.E. Stoller, Direct observation of defect range and evolution in ion-irradiated single crystalline ni and Ni binary alloys, *Sci. Rep.* 6 (2016) 19994.
- [21] M.-R. He, S. Wang, K. Jin, H. Bei, K. Yasuda, S. Matsumura, K. Higashida, I.M. Robertson, Enhanced damage resistance and novel defect structure of CrFe-CoNi under in situ electron irradiation, *Scr. Mater.* 125 (2016) 5–9.
- [22] M.-R. He, S. Wang, S. Shi, K. Jin, H. Bei, K. Yasuda, S. Matsumura, K. Higashida, I.M. Robertson, Mechanisms of radiation-induced segregation in CrFeCoNi-based single-phase concentrated solid solution alloys, *Acta Mater.* 126 (2017) 182–193.
- [23] C. Lu, T. Yang, K. Jin, N. Gao, P. Xiu, Y. Zhang, F. Gao, H. Bei, W.J. Weber, K. Sun, Y. Dong, L. Wang, Radiation-induced segregation on defect clusters in single-phase concentrated solid-solution alloys, *Acta Mater.* 127 (2017) 98–107.
- [24] N.A.P.K. Kumar, C. Li, K.J. Leonard, H. Bei, S.J. Zinkle, Microstructural stability and mechanical behavior of FeNiMnCr high entropy alloy under ion irradiation, *Acta Mater.* 113 (2016) 230–244.
- [25] S. Gorsse, D.B. Miracle, O.N. Senkov, Mapping the world of complex concentrated alloys, *Acta Mater.* 135 (2017) 177–187.
- [26] T. Yang, S. Xia, S. Liu, C. Wang, S. Liu, Y. Zhang, J. Xue, S. Yan, Y. Wang, Effects of Al addition on microstructure and mechanical properties of Al<sub>x</sub>CoCrFeNi high-entropy alloy, *Mater. Sci. Eng. A* 648 (2015) 15–22.
- [27] C. Li, J.C. Li, M. Zhao, Q. Jiang, Effect of aluminum contents on microstructure and properties of Al<sub>x</sub>CoCrFeNi alloys, *J. Alloy Compd.* 504S (0) (2010) S515.
- [28] W.-R. Wang, W.-L. Wang, S.-C. Wang, Y.-C. Tsai, C.-H. Lai, J.-W. Yeh, Effects of Al addition on the microstructure and mechanical property of Al<sub>x</sub>CoCrFeNi high-entropy alloys, *Intermetallics* 26 (0) (2012) 44–51.
- [29] W.R. Wang, W.L. Wang, J.W. Yeh, Phases, microstructure and mechanical properties of Al<sub>x</sub>CoCrFeNi high-entropy alloys at elevated temperatures, *J. Alloy Compd.* 589 (2014) 143–152.
- [30] D. Li, C. Li, T. Feng, Y. Zhang, G. Sha, J.J. Lewandowski, P.K. Liaw, Y. Zhang, High-entropy A<sub>10.3</sub>CoCrFeNi alloy fibers with high tensile strength and ductility at ambient and cryogenic temperatures, *Acta Mater.* 123 (2017) 285–294.
- [31] J.C. Rao, H.Y. Diao, V. Ocelfik, D. Vainchtein, C. Zhang, C. Kuo, Z. Tang, W. Guo, J.D. Poplawsky, Y. Zhou, P.K. Liaw, J.T.M. De Hosson, Secondary phases in Al<sub>x</sub>CoCrFeNi high-entropy alloys: an in-situ TEM heating study and thermodynamic appraisal, *Acta Mater.* 131 (2017) 206–220.
- [32] H.-P. Chou, Y.-S. Chang, S.-K. Chen, J.-W. Yeh, Microstructure, thermophysical and electrical properties in Al<sub>x</sub>CoCrFeNi (0≤x≤2) high-entropy alloys, *Mater. Sci. Eng. B* 163 (3) (2009) 184–189.
- [33] Y.-F. Kao, T.-J. Chen, S.-K. Chen, J.-W. Yeh, Microstructure and mechanical property of as-cast, -homogenized, and -deformed Al<sub>x</sub>CoCrFeNi (0≤x≤2) high-entropy alloys, *J. Alloy Compd.* 488 (1) (2009) 57–64.
- [34] P. Liaw, F. Zhang, C. Zhang, G. Wang, X. Xie, H. Diao, C.-H. Kuo, Z. An, M. Hemphill, Experimental and Computational Investigation of High Entropy Alloys for Elevated-Temperature Applications, Univ. of Tennessee, Knoxville, TN, United States, 2016.
- [35] H.Y. Yasuda, H. Miyamoto, K. Cho, T. Nagase, Formation of ultrafine-grained microstructure in A<sub>10.3</sub>CoCrFeNi high entropy alloys with grain boundary precipitates, *Mater. Lett.* 199 (2017) 120–123.
- [36] Y. Zhang, M.L. Crespiello, H. Xue, K. Jin, C.H. Chen, C.L. Fontana, J.T. Graham, W.J. Weber, New ion beam materials laboratory for materials modification and irradiation effects research, *Nucl. Instrum. Meth. B* 338 (2014) 19–30.
- [37] M.L. Crespiello, J.T. Graham, Y. Zhang, W.J. Weber, Temperature measurements during high flux ion beam irradiations, *Rev. Sci. Instrum.* 87 (2) (2016) 024902.
- [38] R.E. Stoller, M.B. Toloczko, G.S. Was, A.G. Certain, S. Dwaraknath, F.A. Garner, On the use of SRIM for computing radiation damage exposure, *Nucl. Instrum. Meth. B* 310 (2013) 75–80.
- [39] Z. Jiao, G.S. Was, Novel features of radiation-induced segregation and radiation-induced precipitation in austenitic stainless steels, *Acta Mater.* 59 (3) (2011) 1220–1238.
- [40] M.K. Miller, K.F. Russell, K. Thompson, R. Alvis, D.J. Larson, Review of atom probe FIB-Based specimen preparation methods, *Microsc. Microanal.* 13 (6) (2007) 428–436.
- [41] F. Granberg, K. Nordlund, M.W. Ullah, K. Jin, C. Lu, H. Bei, L.M. Wang, F. Djurabekova, W.J. Weber, Y. Zhang, Mechanism of radiation damage reduction in equiatomic multicomponent single phase alloys, *Phys. Rev. Lett.* 116 (13) (2016) 135504.
- [42] K. Jin, W. Guo, C. Lu, M.W. Ullah, Y. Zhang, W.J. Weber, L. Wang, J.D. Poplawsky, H. Bei, Effects of Fe concentration on the ion-irradiation induced defect evolution and hardening in Ni-Fe solid solution alloys, *Acta Mater.* 121 (2016) 365–373.
- [43] S.J. Zinkle, 1.03-Radiation-Induced Effects on microstructure, Comprehensive Nuclear Materials. 1. Basic Aspects of Radiation Effects in Solids, Elsevier, Amsterdam, 2011, pp. 65–98.
- [44] B.L. Eyre, Transmission electron microscope studies of point defect clusters in fcc and bcc metals, *J. Phys. F: Metal Phys.* 3 (2) (1973) 422–470.
- [45] S.J. Zinkle, P.J. Maziasz, R.E. Stoller, Dose dependence of the microstructural evolution in neutron-irradiated austenitic stainless steel, *J. Nucl. Mater.* 206 (2) (1993) 266–286.
- [46] T. Yang, S. Xia, W. Guo, R. Hu, J.D. Poplawsky, G. Sha, Y. Fang, Z. Yan, C. Wang, C. Li, Effects of temperature on the irradiation responses of A<sub>10.1</sub>CoCrFeNi high entropy alloy, *Scr. Mater.* 144 (2018) 31–35.
- [47] S. Takaki, J. Fuss, H. Kuglers, U. Dedeck, H. Schultz, The resistivity recovery of high purity and carbon doped iron following low temperature electron irradiation, *Radiat. Eff.* 79 (1–4) (1983) 87–122.
- [48] C.-C. Fu, J.D. Torre, F. Willaime, J.-L. Bocquet, A. Barbu, Multiscale modelling of defect kinetics in irradiated iron, *Nat. Mater.* 4 (1) (2005) 68–74.
- [49] M.J. Makin, F.J. Minter, Irradiation hardening in copper and nickel, *Acta Metall.* 8 (10) (1960) 691–699.
- [50] B. Singh, A. Horsewell, P. Toft, D. Edwards, Temperature and dose dependencies of microstructure and hardness of neutron irradiated OFHC copper, *J. Nucl. Mater.* 224 (2) (1995) 131–140.
- [51] H.C. Liu, T.E. Mitchell, Defect aggregation in irradiated Ni<sub>3</sub>Al and NiAl, *J. Nucl. Mater.* 107 (2/3) (1982) 318–326.
- [52] S. Fabritsiev, A. Pokrovsky, Effect of irradiation temperature on microstructure, radiation hardening and embrittlement of pure copper and copper-based alloy, *J. Nucl. Mater.* 367 (2007) 977–983.
- [53] S. Zinkle, L. Snead, Microstructure of copper and nickel irradiated with fission neutrons near 230 C, *J. Nucl. Mater.* 225 (1995) 123–131.
- [54] M. Nastar, F. Soisson, Comprehensive Nuclear Materials. 1. Basic Aspects of Radiation Effects in Solids, Elsevier, Amsterdam, 2011.
- [55] L.K. Béland, C. Lu, Y.N. Osetskiy, G.D. Samolyuk, A. Caro, L. Wang, R.E. Stoller, Features of primary damage by high energy displacement cascades in concentrated Ni-based alloys, *J. Appl. Phys.* 119 (8) (2016) 085901.
- [56] C. Lu, L. Niu, N. Chen, K. Jin, T. Yang, P. Xiu, Y. Zhang, F. Gao, H. Bei, S. Shi, Enhancing radiation tolerance by controlling defect mobility and migration pathways in multicomponent single-phase alloys, *Nat. Commun.* 7 (2016) 13564.
- [57] A.J. Zaddach, C. Niu, C.C. Koch, D.L. Irving, Mechanical properties and stacking fault energies of nifecrcmn high-entropy alloy, *JOM* 65 (12) (2013) 1780–1789.
- [58] S. Huang, W. Li, S. Lu, F. Tian, J. Shen, E. Holmström, L. Vitos, Temperature dependent stacking fault energy of FeCrCoNiMn high entropy alloy, *Scr. Mater.* 108 (2015) 44–47.
- [59] A.J. Zaddach, R.O. Scatteringgood, C.C. Koch, Tensile properties of low-stacking fault energy high-entropy alloys, *Mater. Sci. Eng. A* 636 (2015) 373–378.

- [60] J. Liu, C. Chen, Y. Xu, S. Wu, G. Wang, H. Wang, Y. Fang, L. Meng, Deformation twinning behaviors of the low stacking fault energy high-entropy alloy: an in-situ TEM study, *Scr. Mater.* 137 (2017) 9–12.
- [61] X.-X. Wang, L.-L. Niu, S. Wang, Energetics analysis of interstitial loops in single-phase concentrated solid-solution alloys, *J. Nucl. Mater.* 501 (2018) 94–103.
- [62] S.J. Zinkle, N.M. Ghoniem, Operating temperature windows for fusion reactor structural materials, *Fusion Eng. Des.* 51/52 (2000) 55–71.
- [63] Y.-C. Yang, C. Liu, C.-Y. Lin, Z. Xia, Core effect of local atomic configuration and design principles in  $\text{Al}_x\text{CoCrFeNi}$  high-entropy alloys, *Scr. Mater.* 178 (2020) 181–186.
- [64] S.J. Zinkle, L.L. Snead, Opportunities and limitations for ion beams in radiation effects studies: bridging critical gaps between charged particle and neutron irradiations, *Scr. Mater.* 143 (2018) 154–160.
- [65] J.B. Whitley, G.L. Kulcinski, P. Wilkes, H.V. Smith, The depth dependent damage profile in nickel irradiated with nickel or copper ions, *J. Nucl. Mater.* 79 (1) (1979) 159–169.
- [66] J.G. Gigax, T. Chen, H. Kim, J. Wang, L.M. Price, E. Aydogan, S.A. Maloy, D.K. Schreiber, M.B. Toloczo, F.A. Garner, L. Shao, Radiation response of alloy T91 at damage levels up to 1000 peak dpa, *J. Nucl. Mater.* 482 (2016) 257–265.
- [67] T.-n. Yang, C. Lu, K. Jin, M.L. Crespiello, Y. Zhang, H. Bei, L. Wang, The effect of injected interstitials on void formation in self-ion irradiated nickel containing concentrated solid solution alloys, *J. Nucl. Mater.* 488 (2017) 328–337.
- [68] T. Yang, S. Xia, S. Liu, C. Wang, S. Liu, Y. Fang, Y. Zhang, J. Xue, S. Yan, Y. Wang, Precipitation behavior of  $\text{Al}_x\text{CoCrFeNi}$  high entropy alloys under ion irradiation, *Sci. Rep.* 6 (2016) 32146.
- [69] B. Gwalani, V. Soni, D. Choudhuri, M. Lee, J.Y. Hwang, S.J. Nam, H. Ryu, S.H. Hong, R. Banerjee, Stability of ordered L12 and B2 precipitates in face centered cubic based high entropy alloys -  $\text{Al}_{0.3}\text{CoFeCrNi}$  and  $\text{Al}_{0.3}\text{CuFeCrNi}2$ , *Scr. Mater.* 123 (2016) 130–134.
- [70] T.-T. Shun, Y.-C. Du, Microstructure and tensile behaviors of FCC  $\text{Al}_{0.3}\text{CoCrFeNi}$  high entropy alloy, *J. Alloy Compd.* 479 (2009) 157–160.
- [71] Q. Tang, Y. Huang, H. Cheng, X. Liao, T.G. Langdon, P. Dai, The effect of grain size on the annealing-induced phase transformation in an  $\text{Al}_{0.3}\text{CoCrFeNi}$  high entropy alloy, *Mater. Des.* 105 (2016) 381–385.
- [72] C. Abromeit, H. Wollenberger, S. Matsumura, C. Kinoshita, Stability of ordered phases under irradiation, *J. Nucl. Mater.* 276 (1) (2000) 104–113.
- [73] R.A. Enrique, P. Bellon, Compositional patterning in systems driven by competing dynamics of different length scale, *Phys. Rev. Lett.* 84 (13) (2000) 2885.
- [74] R.A. Enrique, P. Bellon, Phase stability under irradiation in alloys with a positive heat of mixing: effective thermodynamics description, *Phys. Rev. B* 60 (21) (1999) 14649.
- [75] S. Shu, N. Almirall, P.B. Wells, T. Yamamoto, G.R. Odette, D.D. Morgan, Precipitation in Fe-Cu and Fe-Cu-Mn model alloys under irradiation: dose rate effects, *Acta Mater.* 157 (2018) 72–82.
- [76] P. Krasnochtchekov, R. Averback, P. Bellon, Homogeneous phase separation in binary alloys under ion irradiation conditions: role of interstitial atoms, *Phys. Rev. B* 75 (14) (2007) 144107.
- [77] J. Ye, P. Bellon, Nanoscale patterning of chemical order induced by displacement cascades in irradiated alloys. I. A kinetic Monte Carlo study, *Phys. Rev. B* 70 (9) (2004) 094104.
- [78] J.M. Gonzalez-Miranda, P.L. Garido, J. Marro, J.L. Lebowitz, Nonequilibrium phase diagram of ISING model with competing dynamics, *Phys. Rev. Lett.* 59 (17) (1987) 1934–1937.
- [79] G. Martin, Phase stability under irradiation: ballistic effects, *Phys. Rev. B* 30 (3) (1984) 1424–1436.
- [80] R.S. Nelson, J.A. Hudson, D.J. Mazey, The stability of precipitates in an irradiation environment, *J. Nucl. Mater.* 44 (3) (1972) 318–330.
- [81] M.H. Mathon, Y. de Carlan, G. Geoffroy, X. Averty, A. Alamo, C.H. de Novion, A SANS investigation of the irradiation-enhanced  $\alpha-\alpha'$  phases separation in 7–12 Cr martensitic steels, *J. Nucl. Mater.* 312 (2/3) (2003) 236–248.
- [82] N.Q. Vo, S.W. Chee, D. Schwen, X. Zhang, P. Bellon, R.S. Averback, Microstructural stability of nanostructured Cu alloys during high-temperature irradiation, *Scr. Mater.* 63 (9) (2010) 929–932.
- [83] R.A. Enrique, K. Nordlund, R.S. Averback, P. Bellon, Nonequilibrium self-organization in alloys under irradiation leading to the formation of nanocomposites, *Nucl. Instrum. Meth. B* 202 (2003) 206–216.
- [84] K.-Y. Tsai, M.-H. Tsai, J.-W. Yeh, Sluggish diffusion in Co-Cr-Fe-Mn-Ni high-entropy alloys, *Acta Mater.* 61 (13) (2013) 4887–4897.
- [85] R. Sizmann, The effect of radiation upon diffusion in metals, *J. Nucl. Mater.* 69 (1978) 386–412.
- [86] G. Odette, G. Lucas, Embrittlement of nuclear reactor pressure vessels, *JOM* 53 (7) (2001) 18–22.
- [87] L.C. Luther, Diffusion along dislocations, *J. Chem. Phys.* 43 (7) (1965) 2213–2218.
- [88] G. Williams Jr, L. Slifkin, Diffusion along dislocations, *Phys. Rev. Lett.* 1 (7) (1958) 243.
- [89] V.E. Wood, M. Glasser, A. Austin, Diffusion along dislocations, *J. Chem. Phys.* 45 (3) (1966) 1079–1080.